

INTERFACE ENGINEERING WITH A THIENOTHIOPHENE-BASED
AMMONIUM SALT FOR REALIZATION OF SEMITRANSSPARENT
PEROVSKITE SOLAR CELLS WITH ENHANCED EFFICIENCY AND
IMPROVED STABILITY

A THESIS SUBMITTED TO
THE GRADUATE SCHOOL OF NATURAL AND APPLIED SCIENCES
OF
MIDDLE EAST TECHNICAL UNIVERSITY

BY

ÜMMÜGÜLSÜM GÜNEŞ

IN PARTIAL FULFILLMENT OF THE REQUIREMENTS
FOR
THE DEGREE OF MASTER OF SCIENCE
IN
CHEMISTRY

SEPTEMBER 2021

Approval of the thesis:

**INTERFACE ENGINEERING WITH A THIENOTHIOPHENE-BASED
AMMONIUM SALT FOR REALIZATION OF SEMITRANSSPARENT
PEROVSKITE SOLAR CELLS WITH ENHANCED EFFICIENCY AND
IMPROVED STABILITY**

submitted by **ÜMMÜGÜLSÜM GÜNEŞ** in partial fulfillment of the requirements
for the degree of **Master of Science in Chemistry, Middle East Technical
University** by,

Prof. Dr. Halil Kalıpçılar
Dean, Graduate School of **Natural and Applied Sciences**

Prof. Dr. Özdemir Doğan
Head of the Department, **Chemistry**

Assoc. Prof. Dr. E. Görkem Günbaş
Supervisor, **Chemistry, METU**

Examining Committee Members:

Prof. Dr. Levent K. Toppare
Chemistry, METU

Assoc. Prof. Dr. E. Görkem Günbaş
Chemistry, METU

Prof. Dr. Ali Çırpan
Chemistry, METU

Assoc. Prof. Dr. Selçuk Yerci
Micro and Nanotechnology, METU

Prof. Dr. Savaş Sönmezoğlu
Metallurgical and Materials Engineering, KMU

Date: 02.09.2021

I hereby declare that all information in this document has been obtained and presented in accordance with academic rules and ethical conduct. I also declare that, as required by these rules and conduct, I have fully cited and referenced all material and results that are not original to this work.

Name Last name : Ümmügülsüm, Güneş

Signature :

ABSTRACT

INTERFACE ENGINEERING WITH A THIENOTHIOPHENE-BASED AMMONIUM SALT FOR REALIZATION OF SEMITRANSSPARENT PEROVSKITE SOLAR CELLS WITH ENHANCED EFFICIENCY AND IMPROVED STABILITY

Güneş, Ümmügülsüm
Master of Science, Chemistry
Supervisor : Assoc. Prof. Dr. E. Görkem Günbaş

September 2021, 76 pages

The stability issues of perovskite solar cells (PSCs) is one of the most important factors preventing commercialization. Various approaches have been proposed to overcome this problem, and among them, interface engineering is highlighted as one of the most convenient ways. In this study, a thienothiophene based ammonium salt (TTMAI) was coated on 3D FAMA ($((\text{FAPbI}_3)_{1-x}(\text{MAPbBr}_3)_x)$)-based perovskite. GIXRD and SEM analysis revealed that TTMAI did not incorporate in the 3D perovskite but only resulted in a change at surface morphology. The solar cells treated with TTMAI showed enhancement in fill factor (FF), increasing their power conversion efficiencies (PCEs) from 17% to over 20%. Moreover, due to the hydrophobic nature of the TTMAI, a remarkable improvement in stability was obtained. The solar cell treated with TTMAI retained 82% of its initial PCE. In comparison, the reference cells maintained only 38% of initial efficiency under 15% humidity for over 380 h. In addition, semitransparent perovskite solar cells (ST-PSC) were fabricated, and 17.9% PCE was achieved with a treated 3D perovskite

stack, which is one of the highest reported efficiencies for FAMA-based 3D perovskites. Additionally, the TTMAI- treated ST-PSC maintained 87% of its initial PCE, whereas 3D only reference retained 69% for six weeks (>1000 h). These results clearly show that this study fills a critical void in perovskite research where highly efficient and stable semitransparent perovskite solar cells are scarce.

Keywords: Interface Engineering, Semitransparent PSC, Hole Extraction, Stability, Novel Organic Spacers

ÖZ

TİYENOTİYOFEN İÇEREN AMONYUM TUZU TEMELLİ ARAYÜZ MÜHENDİSLİĞİ İLE ARTIRILMIŞ VERİMLİLİK VE İYİLEŞTİRİLMİŞ KARARLILIĞA SAHİP YARI ŞEFFAF PEROVSKİT GÜNEŞ HÜCRELERİNİN GERÇEKLEŞTİRİLMESİ

Güneş, Ümmügülsüm
Yüksek Lisans, Kimya
Tez Yöneticisi: Tez Yöneticisi Doç. Dr. E. Görkem Günbaş

Eylül 2021, 76 sayfa

Perovskit güneş pillerinin (PGP'ler) kararsızlık sorunu, ticarileşmelerini engelleyen en önemli faktörlerden biridir. Bu sorunun üstesinden gelmek için çeşitli yaklaşımlar önerilmiştir ve bunlar arasında arayüz mühendisliği en uygun yollardan biri olarak vurgulanmıştır. Bu çalışmada, tiyenotiyofen bazlı amonyum tuzu (TTMAI), 3D FAMA (((FAPbI₃)_{1-x}(MAPbBr₃)_x)) bazlı perovskit üzerine kaplanmıştır. GIXRD ve SEM analizi, TTMAI'nin 3D perovskit dahil olmadığını, sadece yüzey morfolojisinde bir değişikliğe neden olduğunu ortaya koymuştur. TTMAI ile işlenen güneş pilleri, doldurma faktöründe (FF) gelişme göstererek, güç dönüştürme verimliliklerini (GDV'ler) %17'den %20'nin üzerine çıkarmıştır. Ayrıca, TTMAI'nin hidrofobik doğası nedeniyle, stabilitede dikkate değer bir gelişme elde edilmiştir. TTMAI ile işlenen güneş pili, ilk veriminin %82'sini korumuştur. Buna karşılık, referans hücreler 380 saatten fazla bir süre boyunca %15 nem altında ilk veriminin yalnızca %38'ini korumuştur. Ek olarak, yarı saydam perovskit güneş pilleri (YS-PGP) üretilmiştir ve FAMA tabanlı 3D perovskitler için bildirilen en yüksek verimlerden biri olan işlenmiş bir 3D perovskite yığını ile %17,9 verim elde edildi.

Ek olarak, TTMAI ile muamele edilen YS-PGP, ilk GDV'sinin %87'sini korurken, 3D ST-PSC, altı hafta boyunca (>1000 saat) bunun %69'unu korumuştur. Bu sonuçlar, bu çalışmanın, yüksek verimli ve kararlı yarı saydam perovskit güneş pillerinin yetersiz olduğu perovskit arařtırmalarında kritik bir boşluęu doldurduęunu açıkça göstermektedir.

Anahtar Kelimeler: Arayüz Mühendislięi, Yarı Geçirgen Perovskit Güneş Hücreleri, Boşluk Çıkartma, Kararlılık, Özgün Organik Aralayıcılar

To my beloved family...

ACKNOWLEDGMENTS

I would like to express my deepest gratitude to my advisor, Professor Görkem Günbaş, who has always provided his support and guidance throughout my research life. Without his constructive comments, I would not have improved myself and gained my current experience and knowledge. In addition, I am very grateful to Professor Selçuk Yerci for making me more organized through weekly meetings and enabling me to learn precious technical information from him. I would like to thank both of my professors for their trust and patience in me. Without their assistance, I would not have been able to write either the article or my thesis. I would like to thank all members of the FLAIR LAB and Advanced Photonics Photovoltaics (APP). I would like to express my sincere thanks to Dr.Hava Kaya for teaching me the coating techniques with great patience and devotion. I am so fortunate to have had the opportunity to work together at the laboratory. I am very grateful to Dr. Mohsen Ameri for his guidance for hysteresis analysis and manuscript writing. I would like to thank Esra Bağ for her guidance and support in my experiments as well as her valuable companionship. I would like to thank Cem Şahiner for the impedance spectroscopy measurements and Bahri Eren Uzuner for the EQE and absorbance measurements. I am very grateful to Milad Ghasemi for the ITO sputtering. Additionally, I would like to thank my other esteemed teammates Amir Zarean, Benu Çel, Elif Kirdeciler and Zeynep Gözükara for making our working environment enjoyable and for their valuable friendships. It is a great pleasure to work with them. I would like to thank my friends Arman Ayan, Buse Ünlü, Damla Koçak, Gence Bektaş, Milad Ghasemi and Can Özcan for their support and friendship. I would like to thank Cevahir Ceren Akgül for synthesis of the organic spacer. In addition, I am glad to the Central LAB, especially to Dr. İlker Yıldız for UPS, XPS and ARXPS measurements, and Pelin Paşabeyoğlu for GIXRD measurements. I would like to thank the ODTÜ-GÜNAM facility for allowing me to operate several laboratory instruments. I am so thankful to my dear friends Deniz

Şen, Berrin Ayyıldız and Kübra Erden, who are there for me all the time with their valuable friendship and support. I would like to express my heartfelt gratitude to my beloved mother, who has always been by my side and made me the person I am today. I am very grateful to my little sister Zehra Dicle Güneş for empowering me whenever I feel overwhelmed.

TABLE OF CONTENTS

| | |
|--|-----|
| ABSTRACT | v |
| ÖZ..... | vii |
| ACKNOWLEDGMENTS | x |
| TABLE OF CONTENTS | xii |
| LIST OF TABLES | xv |
| LIST OF FIGURES | xvi |
| LIST OF ABBREVIATIONS | xix |
| LIST OF SYMBOLS..... | xxi |
| CHAPTERS | |
| 1 INTRODUCTION..... | 1 |
| 1.1 Brief Introduction to Solar Cells History..... | 1 |
| 1.2 Perovskite Solar Cells..... | 4 |
| 1.2.1 Development of the Perovskite Solar Cells..... | 5 |
| 1.2.2 Device architecture of PSCs..... | 6 |
| 1.3 Semitransparent Perovskite Solar Cells..... | 7 |
| 1.4 Working Principle of Perovskite Solar Cells..... | 10 |
| 1.5 Operation of Perovskite Solar Cells..... | 10 |
| 1.6 Issues and Challenges in PSCs | 12 |
| 1.6.1 Hysteresis | 13 |
| 1.6.2 Stability..... | 13 |

| | | |
|-------|--|-----------|
| 1.7 | Interface Engineering | 15 |
| 1.8 | 2- Dimensional Perovskite Solar Cells..... | 18 |
| 1.9 | 3D/2D Perovskite Solar Cells | 21 |
| 1.10 | Aim of the Thesis..... | 21 |
| 2 | FABRICATION METHODS AND CHARACTERIZATION TECHNIQUES | |
| | 23 | |
| 2.1 | Materials..... | 23 |
| 2.2 | Synthesis of TTMAI and Fabrication of Opaque and Semitransparent Perovskite Solar Cells | 24 |
| 2.3 | Device Characterizations..... | 28 |
| 2.3.1 | Current Density-Voltage (J-V)..... | 28 |
| 2.3.2 | External quantum efficiency (EQE)..... | 29 |
| 2.3.3 | Impedance Spectroscopy..... | 29 |
| 2.4 | Film Characterizations | 30 |
| 2.4.1 | Grazing Incidence X-Ray Diffraction (GIXRD) | 30 |
| 2.4.2 | Scanning Electron Microscopy (SEM) | 31 |
| 2.4.3 | Atomic Force Microscopy (AFM)..... | 31 |
| 2.4.4 | Absorbance | 31 |
| 2.4.5 | Photoluminescence (PL) | 31 |
| 2.4.6 | X-Ray Photoelectron Spectroscopy (XPS) and Angle-Resolved XPS (ARXPS)..... | 32 |
| 2.4.7 | Ultraviolet Photoelectron Spectrophotometry | 32 |
| 2.4.8 | Contact Angle | 32 |
| 3 | RESULTS AND DISCUSSION | 33 |
| 3.1 | Spin rate optimization of the TTMAI ammonium salt..... | 33 |

| | | |
|-------|--|----|
| 3.2 | Concentration Optimization of TTMAI salt | 36 |
| 3.2.1 | Photovoltaic Characterization of the Reference and TT3DP PSCs... | 36 |
| 3.2.2 | Surface characterization of the reference and TT3DP films | 42 |
| 3.3 | Characterizations of the Semitransparent PSCs..... | 52 |
| 3.4 | Stability studies of the opaque and semitransparent solar cells..... | 53 |
| 3.4.1 | Stability Studies of the Opaque PSCs | 53 |
| 3.4.2 | Stability Studies of the ST-PSCs..... | 55 |
| 4 | CONCLUSION | 57 |
| | REFERENCES | 59 |
| | APPENDICES | |
| A. | NMR Results..... | 75 |

LIST OF TABLES

TABLES

| | |
|---|----|
| Table 1.1 Solar cell parameters and stability information of the best performing (i.e., PCE>17%) semitransparent perovskite cells reported in the literature. N ₂ and air storage environments of solar cells are denoted as * and +, respectively. | 8 |
| Table 3.1 Average and the highest device parameters of the reference and TTMAI-treated solar cells..... | 34 |
| Table 3.2 Average and the highest device parameters of the reference and TTMAI-treated solar cells..... | 37 |
| Table 3.3 Hysteresis Index (%) calculations of the reference and the champion TT3DP perovskite solar cells at different scan rates..... | 40 |
| Table 3.4 full width at half maximum (FWHM), and crystallite size parameters obtained from the GIXRD measurements for the reference and TT3DP films | 44 |

LIST OF FIGURES

FIGURES

| | |
|--|----|
| Figure 1.1. Examples of the solar cells types: a)crystalline silicon, b)CIGS, and c)Perovskite, reproduced from ⁷ | 3 |
| Figure 1.2. The comparison between c-Si and Perovskite Solar Cells in terms of a) power conversion efficiency, b)manufacturing cost, c)lifetime, reproduced from ¹ .4 | |
| Figure 1.3. Illustration of the ABX ₃ perovskite crystal structure..... | 5 |
| Figure 1.4. Illustration of the device architectures of PSCs: a) mesoscopic, b) regular planar, c) inverted planar..... | 7 |
| Figure 1.4. The operational process of perovskite solar cells. | 10 |
| Figure 1.6. J-V curve of the solar cell. | 12 |
| Figure 1.7. Reaction pathway of MAPbI ₃ degradation under humidity and illumination..... | 14 |
| Figure 1.8. Degradation reactions of the MAPbI ₃ perovskite at elevated temperatures. | 14 |
| Figure 1.9. Possible surface defects of the perovskite film ⁶³ | 15 |
| Figure 1.10. The interface layers of the perovskite solar cells reproduced from ⁶⁴ .16 | |
| Figure 1.11. Structural illustration of the pure 2D, quasi-2D, and 3D perovskites, reproduced from ⁷⁸ | 19 |
| Figure 1.12. Illustration of the crystallographic planes of 2D perovskite solar cells reproduced from ⁸⁰ | 20 |
| Figure 2.1. The synthesis scheme of TTMAI molecule. | 24 |
| Figure 2.2. Schematics of the thieno[3,2-b]thiophen-2-ylmethanaminium iodide (TTMAI) structure and the illustration of the TT3DP solar cell architecture. | 25 |
| Figure 2.3. Schematic representation of the SnO ₂ layer fabrication. | 26 |
| Figure 2.4. Schematic representation of the perovskite layer fabrication. | 26 |
| Figure 2.5. Schematic representation of the TTMAI layer fabrication. | 27 |
| Figure 2.6. Schematic representation of the Spiro-OMeTAD, MoO _x , and Au layer deposition. | 27 |

| | |
|--|----|
| Figure 2.7. Schematic representation of the ST-PSC fabrication. | 28 |
| Figure 3.1. (a) V_{OC} , (b) J_{SC} , (c) FF, and (d) PCE statistics of reference solar cells and solar cells treated with different spin speeds of TTMAI..... | 34 |
| Figure 3.2. J-V curves of the best-performing reference and TT3DP PSCs..... | 35 |
| Figure 3.3. EQE graphs of the best-performing solar cells..... | 36 |
| Figure 3.4. (a) V_{OC} , (b) J_{SC} , (c) FF and (d) PCE statistics of reference solar cells and solar cells treated with different concentrations of TTMAI..... | 37 |
| Figure 3.5. J-V curves of the best-performing PSCs. | 38 |
| Figure 3.6. Images of the solutions of TTMAI in IPA with different concentrations (From left to right: 3.0 mg/mL, 2.5 mg/mL, and 2.0 mg/mL). | 38 |
| Figure 3.7. EQE spectra of the best performing solar cells. | 39 |
| Figure 3.8. Histogram of reference and TT3DP perovskite solar cells, out of 20 devices..... | 40 |
| Figure 3.9. Absolute hysteresis index graph of the reference and the TT3DP solar cells at different scan rates. | 41 |
| Figure 3.10. Nyquist plot of the reference and TT3DP PSCs..... | 42 |
| Figure 3.11. GIXRD pattern of the reference 3D perovskite, TTMAI-coated glass, $TTMA_2PbI_4$, and perovskite treated with TTMAI (TT3DP). * and ♣ represent diffraction peaks of PbI_2 and 3D perovskite, respectively. The dotted and dashed lines represent the diffraction peak of TTMAI and $TTMA_2PbI_4$ below 10° , respectively. | 43 |
| Figure 3.12. GIXRD patterns of quasi 2D perovskite films prepared from solutions A (TTMAI, MAI, PbI_2 2:1:2), B (TTMAI, MABr, PbI_2 2:1:2) C (TTMAI, MABr, FAI, PbI_2 2:0.5:0.5:2) and D (TTMAI, FAI, PbI_2 2:1:2) letters denote the various composition the of perovskites. The dotted line represents the position of the diffraction peak of TTMAI on the 3D perovskite (TT3DP). | 44 |
| Figure 3.13. GIXRD patterns of 3D perovskite film treated with different concentrations of TTMAI. | 45 |
| Figure 3.14. XPS spectra of the reference and TT3DP films. | 46 |

| | |
|--|----|
| Figure 3.15. Normalized ARXPS spectra for Pb 4f and S 2s signals of the TT3DP film taking different take-off angles. | 46 |
| Figure 3.16. Top-view SEM images of the reference, IPA washed reference and TTMAI (with different concentrations) films. | 47 |
| Figure 3.17. AFM topography images of the reference and TT3DP films. | 48 |
| Figure 3.18. Absorption spectra of the reference and TT3DP films. | 48 |
| Figure 3.19. PL spectra of the reference and TT3DP films..... | 49 |
| Figure 3.20. UPS spectra of the TTMAI film and linear fits to determine the work function and VBM..... | 50 |
| Figure 3.21. Schematic representation of the band-energy diagram of TT3DP perovskite solar cells. | 51 |
| Figure 3.22. Contact angle images of the reference and TT3DP films. | 51 |
| Figure 3.23. J-V curves of the champion reference and TT3DP ST-PSCs. | 52 |
| Figure 3.24. EQE spectra of the reference and TT3DP ST-PSCs. | 53 |
| Figure 3.25. Stabilized PCEs of the reference and TT3DP PSCs measured under continuous light at ambient conditions..... | 54 |
| Figure 3.26. Normalized PCEs of the reference and TT3DP PSCs at ambient conditions. | 55 |
| Figure 3.27. Normalized PCE of the reference and TT3DP ST-PSCs kept under the dark at room temperature with <15% relative humidity for six weeks. | 56 |

LIST OF ABBREVIATIONS

ABBREVIATIONS

| | |
|-----------------|---|
| a-Si | Amorphous silicon |
| A | Absorbance |
| AFM | Atomic Force Microscopy |
| ARXPS | Angle-Resolved X-ray Photoelectron Spectroscopy |
| c-Si | Single crystal silicon |
| m-Si | Multi-crystal silicon |
| CIGS | Copper Indium Gallium Selenide |
| CdTe | Cadmium Telluride |
| DSSC | Dye Synthesized Solar Cells |
| ETL | Electron Transport Layer |
| EQE | External Quantum Efficiency |
| FF | Fill Factor |
| FAMA | Formamidinium Methylammonium |
| GIXRD | Grazing Incidence X-ray Diffraction |
| HTL | Hole Transport Layer |
| HOMO | Highest Occupied Molecular Orbital |
| ITO | Indium doped Tin Oxide |
| IE | Ionization Energy |
| J _{sc} | Short Circuit Current Density |

| | |
|-----------------|--|
| J-V | Current density-Voltage |
| OPV | Organic Photovoltaics |
| PV | Photovoltaic |
| PCE | Power Conversion Efficiency |
| PSC | Perovskite Solar Cells |
| RH | Relative Humidity |
| R | Reflection |
| ST | Semitransparent |
| SEM | Scanning Electron Microscopy |
| SQ | Shockley-Quiesser |
| TCO | Transparent Conductive Oxide |
| T | Transmission |
| TTMAI | Thieno[3,2-b]thiophen-2-ylmethanaminium Iodide |
| tW | Terawatt |
| UPS | Ultraviolet Photoelectron Spectroscopy |
| V _{oc} | Open Circuit Voltage |
| VBM | Valance Band Maximum |
| XPS | X-ray Photoelectron Spectroscopy |
| 3D | 3-Dimensional |
| 2D | 2-Dimensional |

LIST OF SYMBOLS

SYMBOLS

| | |
|-----------|-------------------------------------|
| K | Crystallite shape factor |
| q | Electronic charge |
| λ | Wavelength |
| β | Width of the X-ray diffraction peak |
| Φ | Work function |
| c | Speed of the light |
| θ | Bragg angle |

CHAPTER 1

INTRODUCTION

The exponential increase in world population is quickly leading to the depletion of most of the energy resources. The current global energy demand is 16 TW, and the power demand is expected to exceed 30 TW by 2050.¹ The majority of the global energy demand (more than 80%) is provided by non-sustainable energy resources. However, more than 90% of total global CO₂ emission is caused by the combustion of fossil fuels, resulting in increased environmental pollution and the global warming rate. Therefore, extensive research has been conducted to discover new energy sources to replace fossil fuels. As a result, renewable energy types such as wind, geothermal, solar, and hydroelectric have emerged as an alternative to traditional energy sources.² Since solar energy is the most abundant, cleanest, and directly applicable source, it is one of the most suitable alternatives for powering the planet. The energy generation by using solar power can occur in two pathways. First, solar energy can be used directly in thermal applications to generate power. Second, sunlight can be directly converted to electricity by the photovoltaic effect.³

1.1 Brief Introduction to Solar Cells History

The photovoltaic effect was discovered by the French physicist Becquerel in 1839 by observing an electric current when the metal electrodes, placed in an electrolyte solution, were exposed to light.⁴ The second breakthrough discovery was reported by Adams et al., where they showed that selenium semiconductors are directly exposed to sunlight can generate electricity.⁵ Thereafter, Fritts fabricated the first semiconductor/silicon solar cell by coating selenium on gold to achieve a PCE of 1

% efficiency in 1883.⁶ The first modern silicon solar cells were produced in the Bell laboratories by creating a p-n junction. This development is considered the milestone towards building current state of the art silicon solar cells with efficiencies exceeding 25%.

Solar cells are divided mainly into three categories as the first, second, and third generation. The 1st generation solar cells are wafer-based p-n junction diodes that include single-crystal (c-Si) or monocrystalline silicon and multi-crystal (m-Si), or polycrystalline silicon solar cells. The silicon is an indirect band gap material, so a 1-micrometer thick film to required to produce to absorb adequate sunlight. The wafer-based solar cells dominate 95% of the total PV market share due to their promising efficiency.⁷ In addition, their low decomposition rate ensures owning a long shelf life. However, due to the necessity of high-quality wafers, expensive production processes, and long payback periods, while the following alternatives were being pursued, there has been notable progress in wafer-based silicon solar cell technologies, resulting in significantly lower costs.

The 2nd generation solar cells, produced by thin-film technologies, emerged to reduce the amount of material used in production and fabrication costs without compromising efficiency.⁸ These devices utilized Cadmium Telluride (CdTe), Copper Indium Gallium Selenide (CIGS), or amorphous (a-Si) Silicon as the active layer. Unlike wafer-based Si technologies, direct band gap semiconductor materials and relatively thin films are used in second-generation PVs.

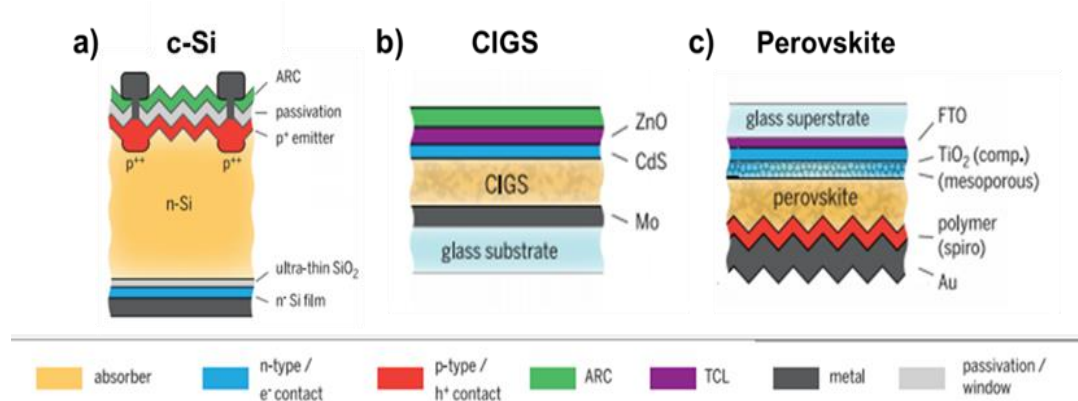


Figure 1.1. Examples of the solar cells types: a)crystalline silicon, b)CIGS, and c)Perovskite, reproduced from ⁹

The third-generation solar cells have emerged to decrease manufacturing costs below second-generation solar cells.¹⁰ They consist of dye synthesized, organic, and perovskite solar cells. O'Regan and Grätzel first reported the dye-sensitized solar cells in the early 1990s as an alternative to p-n junction silicon solar cells with a PCE of 7.9 %.¹¹ Unlike the conventional solar cells, in DSSC structure, dye molecules are utilized as a light-absorbing material placed between electrolytes. In the 2000s, organic solar cells attracted attention due to cheap manufacturing costs and low payback time. However, DSSC and OPV suffered from poor stability and insufficient device performance, causing them to lag far behind conventional power generators. In 2009, perovskite solar cells emerged with the utilization of perovskite crystal as a light-harvesting material at DSSC (Figure 1.1). Perovskite solar cells are promising candidates for cell applications due to their superior optical and electrical properties such as long diffusion length, high charge carrier mobility, narrow band gap, and high absorption coefficient.¹²⁻¹⁶ As shown in Figure 1.2, within a decade, the PCE of the perovskites has reached silicon solar cells at half the cost of the that of silicon solar cell manufacturing.¹⁷

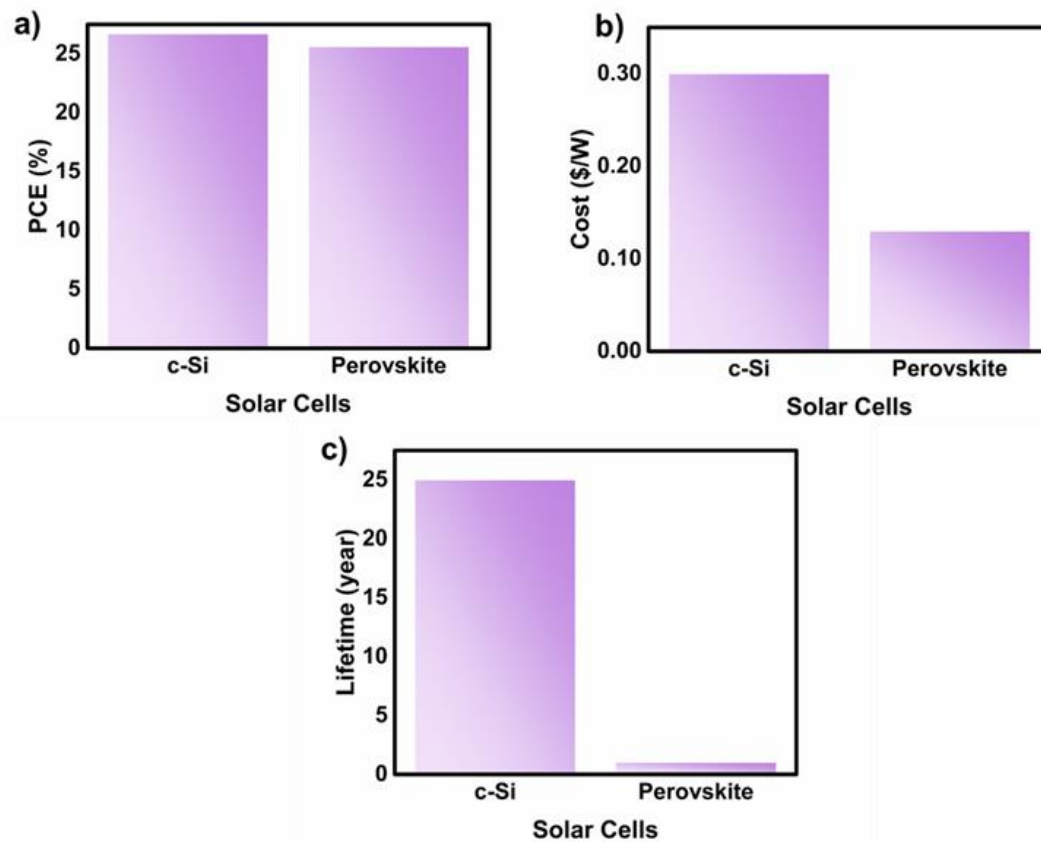


Figure 1.2. The comparison between c-Si and Perovskite Solar Cells in terms of a) power conversion efficiency, b) manufacturing cost, c) lifetime, reproduced from. ¹

1.2 Perovskite Solar Cells

Perovskite is a CaTiO_3 mineral discovered in the Ural Mountains by Gustav Rose in 1839 and named after Russian mineralogist L.A. Perovski. It has a general formula of ABX_3 in which A is a small monovalent cation (CH_3NH_3^+ , $\text{C}_2\text{H}_5\text{N}_2^+$, Cs^+ , Rb^+) occupying the cavities within the lattice. B is an inorganic cation (Pb^{+2} , Sn^{+2}), and X is a halide (I^- , Cl^- , Br^-), and they form $[\text{PbX}_6]^{-4}$ corner-sharing octahedra, which are bound together with A cations (Figure 1.3).¹⁸

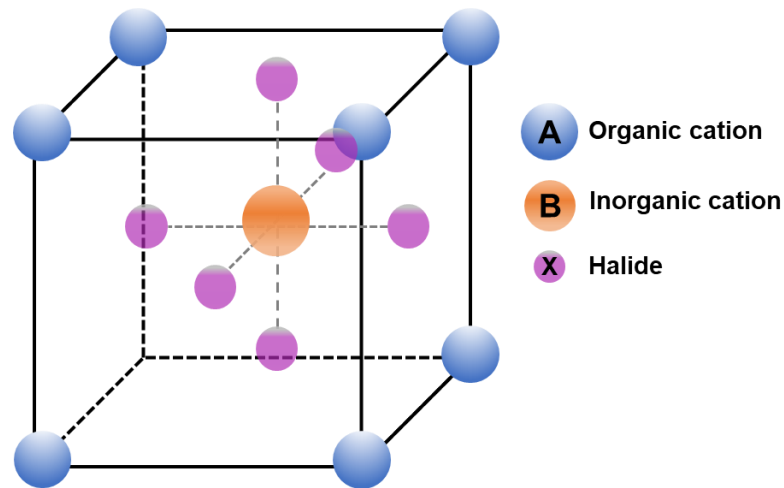


Figure 1.3. Illustration of the ABX₃ perovskite crystal structure.

The Goldschmidt tolerance factor (t) determines the structural stability of perovskites in which R_A , R_B , and R_X represent the ionic radii of the A, B, and X ions, respectively. The t is 1 for an ideal packed cubic system. However, the tolerance factor between $0.8 \leq t \leq 1$ is sufficient for obtaining stable 3D cubic perovskite structures. When the tolerance factor is less than 0.8, tetragonal or orthorhombic structures are likely to be formed.¹⁹

$$t = \frac{R_A + R_X}{\sqrt{2}(R_B + R_X)} \quad (1.1)$$

The perovskite structure (MAPbI₃) has an optical band gap of 1.57 eV and can be easily tuned from 1.2 eV to 3.0 eV by halide incorporation (Br⁻ and Cl⁻).²⁰ Perovskite compounds are direct band gap materials.

1.2.1 Development of the Perovskite Solar Cells

In 2009, Miyasaka and his group demonstrated nanocrystals of methylammonium lead triiodide (MAPbI₃) perovskite as a liquid sensitizer in the dye-sensitized solar cells (DSSC), achieving a power conversion efficiency (PCE) of 3.81%.²¹ Subsequently, Park and colleagues used perovskite quantum dots as a sensitizer

with a similar device architecture in DSSC. However, the stability of the absorber layer suffered from instability due to rapid degradation in the liquid electrolyte.²² Therefore, to overcome the stability problem, solid-state perovskites had been discovered. In 2012, two breakthrough reports were published; Park, Grätzel, and colleagues replaced a liquid electrolyte with the solid-state hole transport material, named 2,2',7,7'-Tetrakis[N,N-di(4-methoxyphenyl)amino]-9,9'-spirobifluorene (Spiro OMeTAD).²³ It is not only improved the stability of the cells but also increased the PCE up to 9.7%. In the second study, Snaith and his co-workers replaced the TiO₂ nanoporous layer with a non-conductive Al₂O₃ and developed mixed-halide CH₃NH₃PbI_{3-x}Cl_x perovskite boosted the efficiency to 10.9%.²⁴ In 2013, a vacuum deposition technique was developed, and more uniform films were obtained with MAPbI_{3-x}Cl_x structure achieving a PCE of over 15%.²⁵ In 2014, the two-step solution method was demonstrated by Im et al., achieving a PCE of 17.01%. They reported that the crystal size of the MAPbI₃ perovskite depends on the exposure time of PbI₂ to MAI.²⁶ The Li doped mesoporous titania was utilized in 2015 with negligible hysteresis loss. It has been reported that Li doping improved the electronic properties of the layer and showed fast electron transport properties.²⁷ New approach for perovskite film fabrication was demonstrated by Bi et al.. They inserted poly(methyl methacrylate) (PMMA) into the antisolvent to control nucleation and crystal growth of perovskite crystals, the study resulted in improved stability and high reproducibility..²⁸ As a result of the improvements, the PCE of perovskite solar cells increased up to 25.6% in 2021.²⁹

1.2.2 Device architecture of PSCs

As mentioned earlier, the first perovskite solar cell was fabricated based on the DSSC architecture. As seen in Figure 1.4, the PSCs can be classified as mesoscopic, regular planar (nip), and inverted planar (pin) structures.³⁰ The typical nip devices consist of glass-coated transparent conductive oxide (TCO), the electron transport layer (ETL), the light-absorbing layer, the hole transport layer (HTL), and the metal top electrode.

The mesoporous structure originated from DSSCs,³¹ and planar PSC evolved from a mesoscopic network 10. Unlike regular PSCs, the inverted planar structures have the opposite configuration of ETL and HTL. Typically, indium-doped tin oxide (ITO) and fluorine-doped tin oxide (FTO) are used as TCO; PEDOT: PSS, nickel oxide (NiO_x), Spiro OMeTAD, and CuSCN are often used as HTMs; titanium dioxide (TiO₂) and tin oxide (SnO₂) are utilized as ETMs; and aluminum, gold, and silver are preferred as top metal electrodes in PSCs.

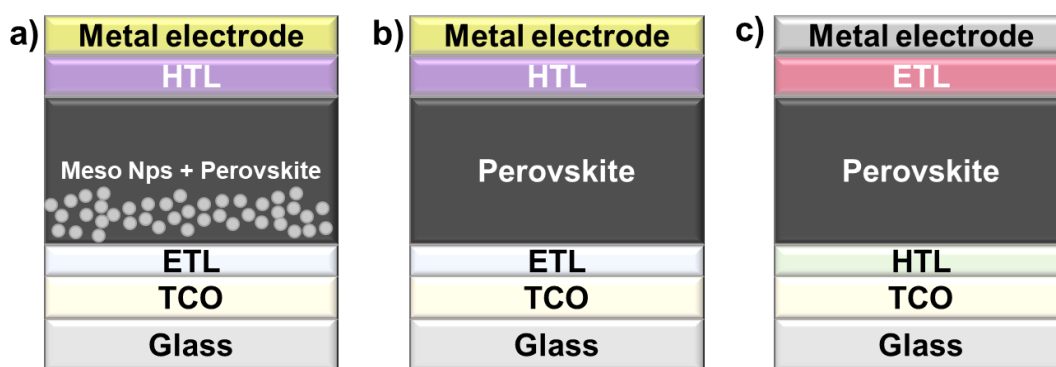


Figure 1.4. Illustration of the device architectures of PSCs: a) mesoscopic, b) regular planar, c) inverted planar.

1.3 Semitransparent Perovskite Solar Cells

Semitransparent solar cells are of great attention due to the wide range of application fields, including power-generating windows on buildings or automobiles and flexible wearable electronics.^{32,33} In addition, semitransparent perovskite solar cells (ST-PSCs) are also of interest for their role in the realization of tandem solar cells and their potential to be integrated into windows in buildings, such as the commercial semitransparent cells.³⁴

ST-PSCs are fabricated by replacing metal top electrodes of opaque PSCs with transparent electrodes. The transparency of the electrodes is vital for the device performance of ST-PSC. Various materials including, TCOs, silver nanowire, graphene, and PEDOT: PSS, have been utilized successfully in ST-PSC fabrication

as transparent electrodes.²⁰ Among them, transparent conductive oxides, including ITO, aluminum-doped zinc oxide (AZO),³⁵ hydrogen-doped indium oxide ($\text{In}_2\text{O}_3:\text{H}$),³⁶ and indium-doped zinc oxide (IZO), is the most promising electrodes to provide excellent transparency (in the visible and near-infrared region) required for high device performance.³⁷ However, their production is accomplished by magnetron sputtering, which can damage the underlying perovskite or organic transport layer. Therefore, a suitable transition metal oxide is required to protect the underlying layers.³⁸ For this purpose, molybdenum oxide (MoO_x or MoO_3) is an extensively used buffer layer.

Several studies have been reported with ST-PSCs, and the solar cells with the highest device performances are listed in Table 1.1.

Table 1.1 Solar cell parameters and stability information of the best performing (i.e., PCE>17%) semitransparent perovskite cells reported in the literature. N_2 and air storage environments of solar cells are denoted as * and +, respectively.

| Device Structure | V_{oc} (V) | J_{sc} (mA/cm ²) | FF (%) | PCE (%) | Active Area (mm ²) | Stability | Ref |
|--|--------------|--------------------------------|--------|---------|--------------------------------|---|---------------|
| Glass/ITO/SnO₂/Cs_{0.05}FA_{0.95}PbI₃/Spiro-OMeTAD/Cr/Au/MgF₂ | 1.14 | 21.9 | 79.7 | 19.8 | 100 | Storage in dark ⁺ for 60 days Retained PCE: ~80% | ³⁹ |
| Glass/IZrO/SnO₂ / Cs_{0.05}FA_{0.81}MA_{0.14}PbI_{2.55}Br_{0.45}/Spiro-OMeTAD/MoO_x/IZO/MgF₂/Ag | 1.12 | 22.3 | 77.7 | 19.4 | 4.90 | MPPT under continuous illumination* for 100h Retained PCE: 75% | ⁴⁰ |

Table 1.1 (Cont'd)

| | | | | | | | |
|---|------|-------|------|-------|------|--|---------------|
| FTO/bl-TiO₂/m-TiO₂/(FAPbI₃)_{1-z}(MAPbBr₃)_z/PTAA/WO_x/NbO_y-AR/ITO/Au fingers | 1.02 | 23.5 | 78.8 | 18.9 | 7.00 | MPPT under continuous illumination n ⁺ for 100h Retained PCE: 90% | ⁴¹ |
| Glass/ITO/TiO₂/MAPbI₃/Spiro-OMeTAD/MoO₃/Au/MoO₃ | 1.16 | 19.8 | 79.9 | 18.3 | 9.60 | Storage in the dark ⁺ for 172 h Retained PCE: 95% | ⁴² |
| ITO/C₆₀/MAPbI₃-_xBr_x/Spiro-OMeTAD/MoO₃/Au/MoO₃ | 1.07 | 22.4 | 73.0 | 17.5 | 7.57 | N/A | ⁴³ |
| Quartz/ITO/c-TiO₂/m-TiO₂/Rb_{0.05}Cs_{0.095}MA_{0.1425}FA_{0.7125}PbI₂Br /n-BABr/Spiro-OMeTAD/MoO_x/IZO | 1.21 | 18.0 | 78.9 | 17.1 | 21.0 | MPPT under continuous illumination n* for over 100h Retained PCE: 94% | ⁴⁴ |
| ITO/NiO_x/4-bromobenzoin acid/ Perovskite /LiF/C60/SnO_x/IZO | 1.15 | 19.99 | 78.7 | 18.04 | 103 | MPP: 40 °C 500 h Thermal: 85 °C ~1000h | ⁴⁵ |
| ITO/CuSCN/CH₃NH₃PbI₃/PC₆₀BM /np-ZnO:Al nps. /AgNW | 1.10 | 21.00 | 74.1 | 17.1 | 100 | N/A | ⁴⁶ |

1.4 Working Principle of Perovskite Solar Cells

Solar cells operate in three steps: absorption of the light, charge generation, and charge collection. Firstly, absorber material is excited by a photon with more energy and creates exciton (electron-hole pair) when exposed to sunlight.⁴⁷ The high absorption coefficient of the PSCs allows them to absorb incident light with a thin perovskite layer.⁴⁸ Secondly, the dissociation of excitons into electrons and holes occurs due to the perovskite's low binding energy and is followed by a migration of the photogenerated electrons and holes to the Perovskite/ETL and Perovskite/HTL interfaces under the effect of the electric field.⁴⁹ The perovskite's long charge carrier diffusion length provides efficient charge extraction even in the thicker active layers. Then, carriers are transported and collected in the electrodes. Finally, the transparent conductive oxide (TCO) layer and metal contacts are connected to produce photocurrent.⁵⁰

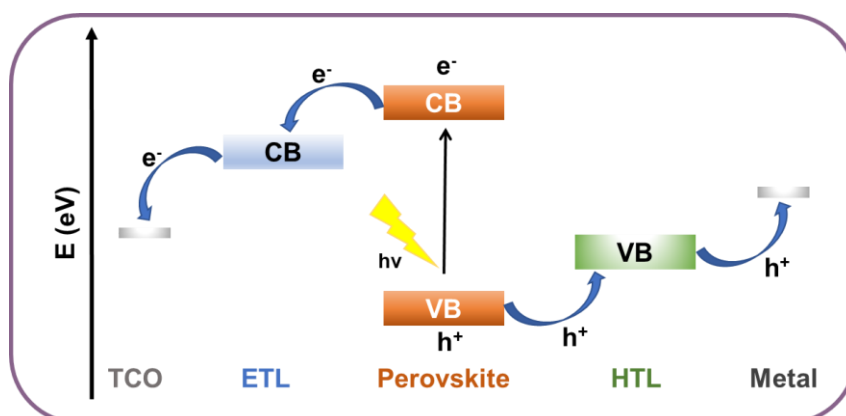


Figure 1.5. The operational process of perovskite solar cells.

1.5 Operation of Perovskite Solar Cells

The solar cell parameters are strongly affected by the intensity of the coming light and the power of the spectrum. Therefore, the operation must occur under standard test conditions (STC) for precise measurements of the device parameters. According

to STC, the total solar irradiance on the solar cell should be 100 mW/s^2 (i.e., one sun) with an Air Mass 1.5 spectrum and operate under a temperature of $25 \text{ }^\circ\text{C}$.

The device performance of the perovskite solar cells is assessed by the current density-voltage (J-V) graph. Power conversion efficiency (PCE) of the solar cells depends on several parameters, including short circuit current density (J_{SC}), open-circuit voltage (V_{OC}), and fill factor (FF), which can be interpreted from the J-V curve. The J_{SC} is the ratio of short circuit current (I_{SC}) to the active area of the solar cell. The I_{SC} is the current flow through the circuit when the solar cell is short-circuited (i.e., when the voltage is zero). V_{OC} is defined as the maximum voltage at which the net current through the solar cell equals zero⁵¹. The FF is the ratio of the maximum power of the solar cell to the product of V_{OC} and J_{SC} . The formula of FF is given in Equation 1.3.

$$FF = \frac{V_{max} \times J_{max}}{V_{OC} \times J_{SC}} \quad (1.2)$$

FF equals one in the ideal solar cells, and as it deviates from the ideality, the device performance decreases. FF is directly affected by parasitic resistances (series and shunt resistance). The series resistance (R_S) in the solar cells is mainly due to the resistance of the top and rear metal contacts, the resistance between the contact resistance between the top metal contact and the transport layer, and the current movement through the transmitter and base of the solar cells.⁵² Shunt resistance (R_{Sh}), parallel resistance, is the microscopic defects in the solar cells that arise during the fabrication process, providing an alternative path to the photogenerated current. The R_S should be as small as possible, and R_{Sh} should be high to approach an ideal solar cell performance.

The PCE is calculated by dividing the maximum output power obtained from the solar cells by the incident power of the sun. The formula is given in equation 1.3.

$$PCE = \frac{P_{OUT}}{P_{IN}} = \frac{V_{OC} \times J_{SC} \times FF}{P_{IN}} \quad (1.3)$$

The incident power is taken as 100 mW/cm^2 in PCE calculations.

Another critical parameter that the J-V curve can interpret is the maximum power point (MPP), defined as the maximum power that solar cells could reach during operation. The J-V curve is given in Figure 1.6.

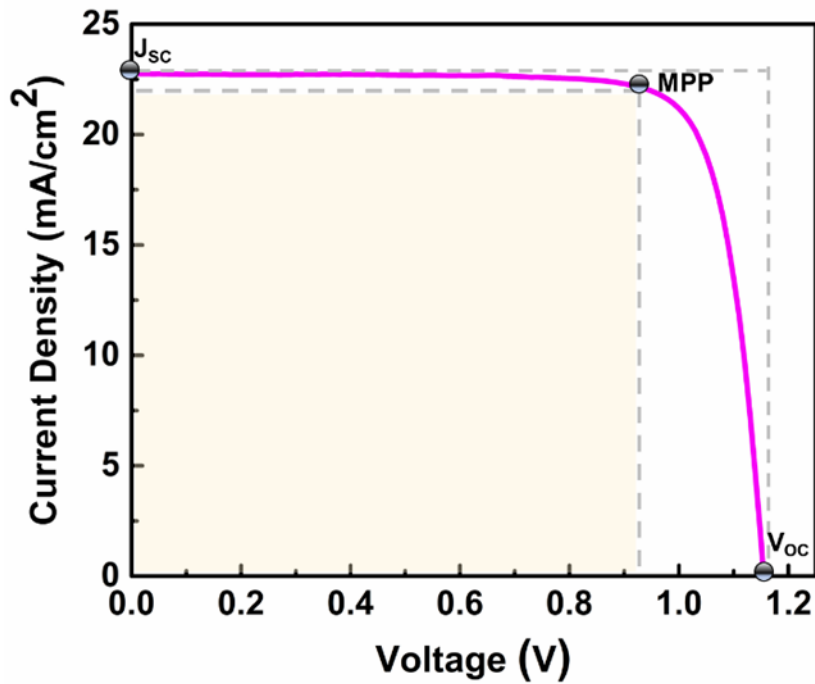


Figure 1.6. J-V curve of the solar cell.

1.6 Issues and Challenges in PSCs

As mentioned earlier, perovskite solar cells have become a major competitor for solar cells dominating the PV market due to their superior device performance. However, besides their remarkable performance, nearly all PSCs suffer from hysteresis during J-V measurements. Moreover, they do not provide the required stability for commercialization. Insufficient operational stability of PSCs due to decomposition patterns related to moisture⁵³, oxygen⁵⁴, UV-light⁵⁵, and heat⁵⁶ hinder the up-scaled development for commercialization.

1.6.1 Hysteresis

J-V hysteresis, which expresses the difference in efficiency between forward and reverse scanning directions of J-V measurements,⁵⁷ is one of the major concerns hindering the further development of PSCs. There are two types of hysteresis, normal and reverse. In normal hysteresis, the efficiency in the reverse scan is higher than the forward scan, while this is the opposite in reverse hysteresis. Although the leading cause of hysteresis is still controversial, it is known that ion migration, ferroelectric polarization, ion accumulation, ambient temperature, capacitive effects,⁵⁸ device architecture, and scan rate are responsible for the hysteresis of PSCs.⁵⁹

1.6.2 Stability

Solar cells must pass several aging tests such as light soaking at elevated temperatures, temperature cycling (-40 to 85 °C), thermal and relative humidity (RH) tests (85 °C/85 RH or 85/85 DH) to be commercialized.⁶⁰ In addition, according to standards of thin-film photovoltaic cells (IEC 61646 climatic chamber tests), their power conversion efficiencies losses must be a maximum of 10% of their initial yields over a period of 1000 h.⁶¹ The lifetime of the silicon solar cells exceeds 25 years, whereas, for the PSCs, the highest shelf-life stability was reported as one year. As previously stated, PSCs tend to degrade under humidity, light soaking, and high-temperature conditions.

The irreversible degradation of the perovskite structure occurs when it is exposed to humidity coupling with direct illumination. Firstly, MAPbI₃ degrades into lead iodide (PbI₂) and methylammonium iodide (CH₃NH₃I) and follows by further decomposing methylammonium iodide (MAI) to methylammonium (CH₃NH₂) and hydroiodic acid (HI). Finally, HI is oxidized with oxygen, or it can be excited by light and produce hydrogen gas (H₂) and iodine (I₂) (Figure 1.7).⁶²

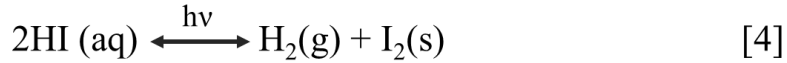
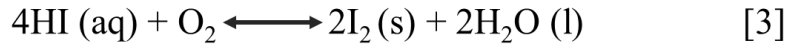
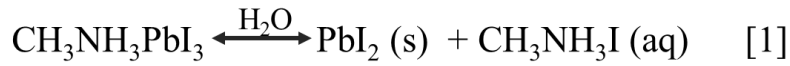


Figure 1.7. Reaction pathway of MAPbI₃ degradation under humidity and illumination.

The solar cell must have the ability to withstand operational temperatures (from -40 °C to 85 °C). In general, the source of instability in perovskites is primarily due to the organic cations. It was reported that MAPbI₃ perovskite degrades at elevated temperatures (85 °C) into several side products, including PbI₂ with MA and HI (volatile compounds) or with ammonia (NH₃) and methyl iodide (CH₃I),⁶³ and one of the reactions in Figure 1.8 occur.⁵⁶

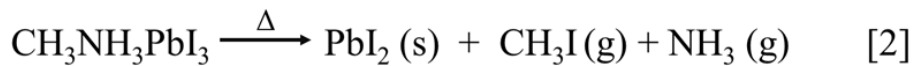


Figure 1.8. Degradation reactions of the MAPbI₃ perovskite at elevated temperatures.

Various aspects of strategies have been demonstrated to improve the stability of the perovskite solar cells, such as interface modification, solvent engineering, compositional engineering, and encapsulation.⁶⁴ It has been concluded that interface engineering and perovskite dimensionality reduction are promising techniques.

1.7 Interface Engineering

Interface engineering is an effective way to improve the device performance and stability of the perovskite solar cells by tuning the interfaces to minimize interfacial losses.

The Shockley-Quiesser (SQ) limit defines the maximum theoretical efficiency that photovoltaics could reach. This efficiency limit is defined as 31% for single-junction PSCs and 33.2% for perovskite-perovskite tandem solar cells.^{65,66} However, the efficiency of the PSCs is still far behind SQ, possibly due to interfacial losses arising from ionic defect states such as under-coordinated ions (Pb^{+2} and I^-), halide, and organic cation vacancies that are likely to exist in the perovskite bulk (Figure 1.9).⁶⁷ These defects are mainly responsible for the formation of nonradiative combination centers,⁶⁸ which hinders further development of device performance of the PSCs. In addition, misaligned energy levels are also another cause for interface-induced recombinations. In addition to stability, the point defects also have a detrimental effect on solar cell stability. Thereby, the passivation of the defects by introducing an appropriate interface layer is pivotal to reduce the nonradiative recombination.

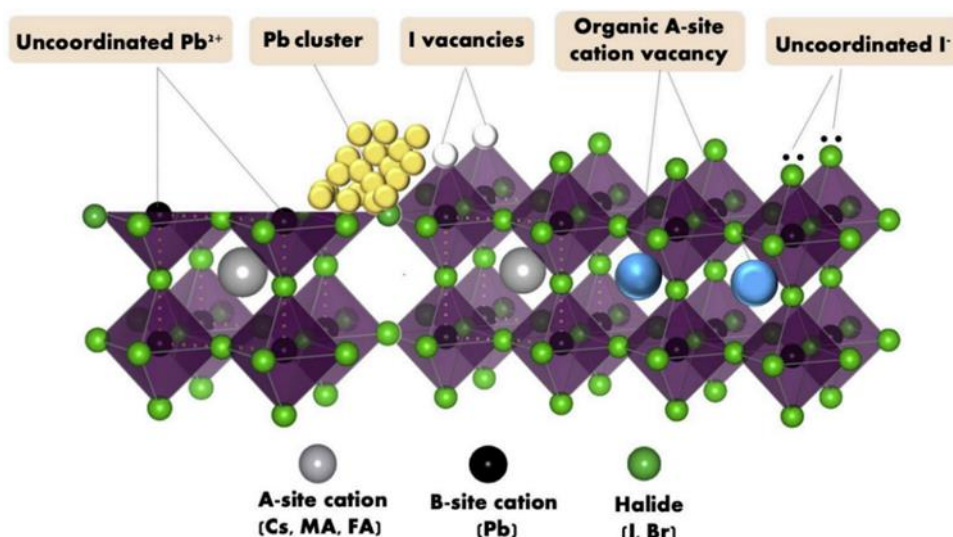


Figure 1.9. Possible surface defects of the perovskite film.⁶⁹

Perovskite solar cells have four interface regions located between TCO-ETL, ETL-absorbing layer, perovskite-HTL, and HTL-metal contact, as shown in Figure 1.10. ETL/perovskite and perovskite/HTL interfaces play a key role in enhancing device parameters, especially V_{OC} and J_{SC} .

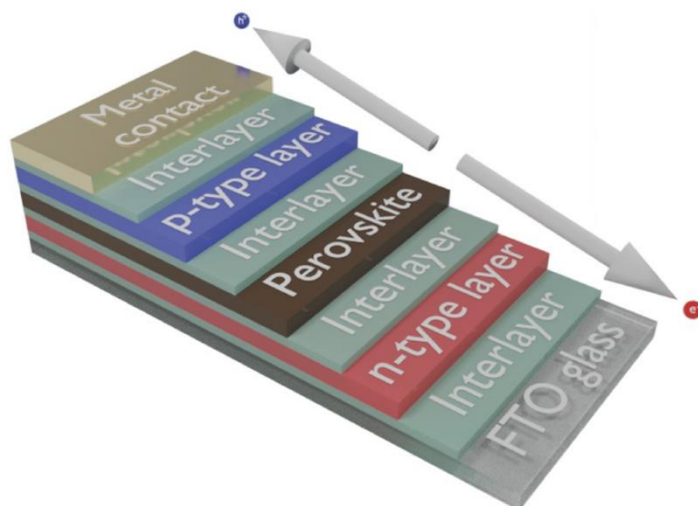


Figure 1.10. The interface layers of the perovskite solar cells reproduced from ⁷⁰.

Interface engineering can improve device performance in several ways. It can be utilized to improve the perovskite absorber or modify band energy levels to suppress recombination and enhance charge transportation. In addition, it can be used to improve device stability. ⁷⁰

Polymers, small molecules, metal oxides, and graphene-based compounds are generally realized as interface modifiers. Among them, small molecules attract great attention due to their low cost and easy synthesis procedures. ⁷⁰ Organic ammonium salts (Lewis acids and bases) have become excellent passivating agents due to their ability to reduce recombination velocity by neutralizing charged ionic defects on perovskite surfaces by chemical passivation. ⁷¹

Additionally, thiophene-based molecules are heavily preferred as a modifier because lone pairs on the thiophene rings can make bonds with the under-coordinated Pb^{+2} sites on the perovskite surface, decrease trap densities, reduced carrier recombination ⁷², and enhance charge extraction properties.

Noel et al. first demonstrated Lewis bases (thiophene and pyridine) as interfacial modifiers on perovskite surface and reported that sulfur and nitrogen atoms on Lewis bases could passivate under-coordinated Pb^{2+} defects via coordination bond, resulting in a significant increase in carrier lifetime and improved device performance.⁷³ Wen et al. introduced a 3-hexylthiophene layer between the absorber and HTL. Due to the high delocalization of the π electrons in the thiophene ring, the treated cells achieved better charge transport and collection at the interfaces. Moreover, superior hydrophobicity of the thiophene-based molecule improved the device's stability; the solar cells retained more than 80% of their initial efficiency under ambient conditions for 700 h.⁷⁴ Lin et al. utilized π -conjugated Lewis base (indacenodithiophene end-capped with 1,1-dicyanomethylene-3-indanone (IDIC)) into the PSCs. It has been reported that the IDIC molecule passivates the Pb clusters located at the surface and the grain boundaries of the perovskite, resulting in better electron extraction and transport. Significant enhancement in open-circuit voltage and photocurrent was observed in addition to improvement in the stability.⁷⁵ Park and his co-workers reported another study by demonstrating a 2-(2-aminoethyl)thiophene hydroiodide (2-TEAI) molecule between the perovskite and novel hole transport layer (HL38) and achieving a PCE above 21% with notable thermal stability. The modified solar cells maintained 85.9% of their initial for 1000 h at 85 °C while PCE of the control cell dropped from 21.1% to 5.8%.⁷⁶

Interface engineering can also provide desirable energy band alignment between perovskite and the transport layers, resulting in improved carrier transport properties and device performances. The highest unoccupied molecular orbital (HOMO) level of the interface layer, positioned at the perovskite/HTL interface, should lie between the absorber material valence band and the HOMO level of the hole transport material for better charge transportation.⁷⁷ Another efficacious method to provide better PCE and stability of the PSCs is forming 2-dimensional (2D) perovskites.

1.8 2- Dimensional Perovskite Solar Cells

The first low dimensional (2D) perovskite structure was demonstrated by Dolzhenko et al. in 1986.⁷⁸ Its application on solar cells was realized in 2014 with PEAI large cation, achieving a PCE of 4.73% by Karunadasa and co-workers.⁷⁹ Furthermore, the 2D PSCs power conversion efficiency increased up to 20% with a remarkable open-circuit voltage of 1.223 V.⁸⁰

Unlike 3D systems, 2D perovskites contain an organic cation (A') larger than the tolerance factor of the cavity created by the inorganic counterparts, thus constraining the continuous 3D lattice.^{81,82} The bonds between small organic cations and $[\text{PbX}_6]^{-4}$ are broken, and large organic cations intercalate between $\text{A}_{n-1}\text{B}_n\text{X}_{3n+1}$ conducting sheets.

Low dimensional perovskites have a generic formula of $(\text{A}')_m\text{A}_{n-1}\text{B}_n\text{X}_{3n+1}$. The large organic cation can be either monovalent ($m=2$) or divalent ($m=1$). For the Ruddlesden Popper phase, the general chemical formula is $(\text{A}')_2\text{A}_{n-1}\text{B}_n\text{X}_{3n+1}$, and “n” defines the thickness of the inorganic slabs in which $n=1$ expresses a pure 2D layer, $2 < n < \infty$ represents quasi-2D, and $n=\infty$ corresponds to a 3D perovskite (Figure 1.11). Thickness can be tuned by adjusting a stoichiometric ratio of the small cations and large organic cations.⁸³ A' is an organic spacer that can be aromatic or aliphatic ammonium cation.

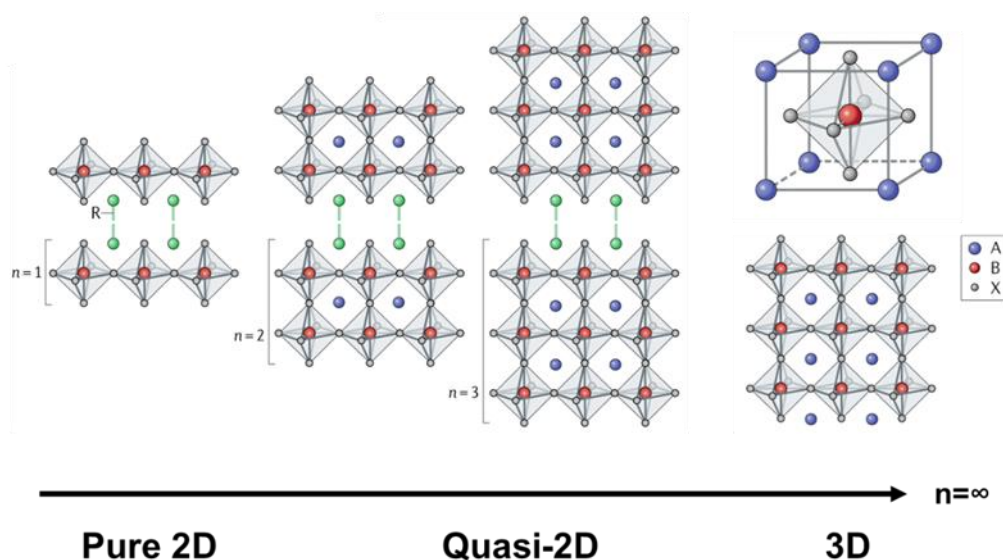


Figure 1.11. Structural illustration of the pure 2D, quasi-2D, and 3D perovskites, reproduced from.⁸⁴

Low dimensional crystalline perovskite structure is obtained by cutting along the corresponding 3D perovskite from specific crystallographic planes. They can be formed in three different directions as $\langle 100 \rangle$, $\langle 110 \rangle$ or $\langle 111 \rangle$ (Figure 1.12). The $\langle 100 \rangle$ -oriented perovskite structures are far the most extensively studied among others, and they can be further classified as the Ruddlesden Popper, Dion Jacobson, and Aurivillius phases. Among them, the Ruddlesden-Popper phase is the most commonly utilized in solar cell applications. On the other hand, a few reports were published with $\langle 110 \rangle$ -oriented crystals with a general formula of $(A')_2A_{m-1}B_mX_{3m+2}$. They are derived by cutting along the face diagonal of the 3D perovskite. However, the difficulty of adjusting the thickness of the inorganic layers limits their use in solar cell applications. In addition, highly symmetrical and small organic cations are required to stabilize the lattice, but very few molecules have these properties. Finally, $\langle 111 \rangle$ -oriented family, more rarely reported, has a chemical formula of $(A')_2A_{q-1}B_qX_{3q+3}$. They are obtained by cutting the main 3D structure along the body diagonal, which causes a B-site deficiency and consequently prevents the formation of 2D compounds in a $\langle 111 \rangle$ -orientation.⁸⁵

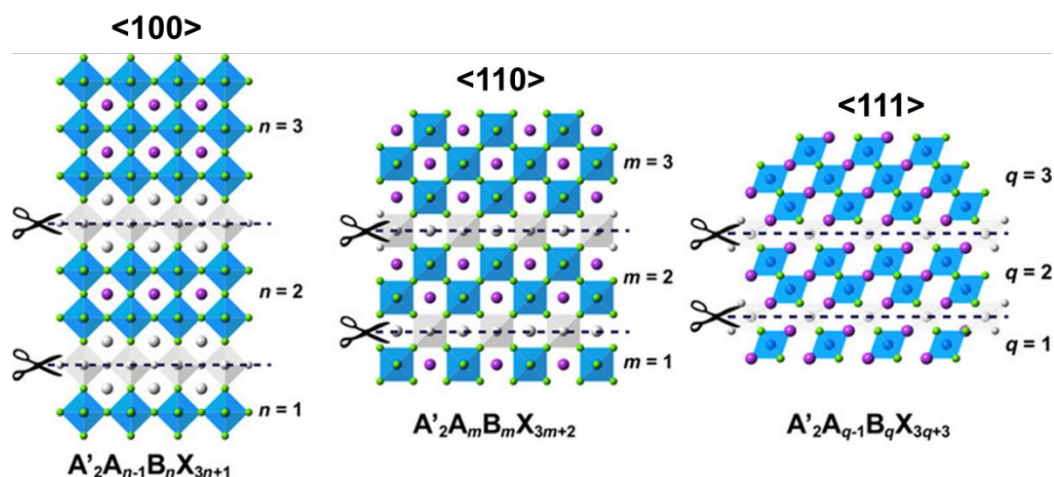


Figure 1.12. Illustration of the crystallographic planes of 2D perovskite solar cells reproduced from.⁸⁶

Contrary to <100>-oriented structures, $n=1$ compounds correspond to 2D perovskite, whereas for <110>-oriented family, $m=1$ corresponds to the formation of the chain-like 1D structure, and for <111>-oriented structure, $q=1$ compounds indicates the formation of a 0D layer.⁸⁷

Low dimensional perovskites are designed to prevent the penetration of water molecules into 3D film and suppress ion migration. Moreover, compared to 3D perovskites, 2D perovskites have no size limitation, indicating that they can have a wide range of molecular designs, such as the large organic cation containing a long alkyl chain or diammonium cations. Although 2D perovskites are more advantageous than 3D counterparts in terms of stability enhancement, their efficiencies are still far behind their competitors due to having high exciton binding energy and low absorption coefficient.⁸⁸⁻⁹⁰ Therefore, 3D/2D perovskite solar cells have been demonstrated to produce solar cells with enhanced efficiency and improved stability.

1.9 3D/2D Perovskite Solar Cells

The 3D / 2D concept was first introduced by C.Ma et al. in 2016 using the $CA_2PbI_4/MAPbI_xCl_{3-x}$ structure. 2D layer (CA_2PbI_4), obtained by reaction of cyclopropylammoniumiodide (CAI) with excess PbI_2 on the 3D film surface, not only enhanced the PCE but also showed remarkable stability over 40 days without any degradation and maintained more than 50% of its initial PCE at a relative humidity of $63 \pm 5\%$ for 220 h. In contrast, the 3D PSC degraded dramatically and lost all its efficiency at the end of 50 h.⁹¹ A year later, aminovaleric acid iodide ($HOOC(CH_2)_4NH_3$), i.e., AVAI) was utilized in a 3D/2D solar cell with the configuration of glass/FTO/c-TiO₂/m-TiO₂/3D perovskite/2D layer/Spiro-OMeTAD /Au by Graccini et al. with a PCE of 12.9%. It showed excellent moisture stability for a year (12000 hours) without compromising any efficiency loss and still has the highest stability among all perovskite solar cells.⁹² Various organic ammonium salts with different structures have been used to fabricate 3D/2D cells.⁹³⁻⁹⁸ Recently, researchers have turned their attention to molecules containing chalcogens, especially sulfur, which provide high polarizability and strong intermolecular interactions, thus improving charge transport properties.⁹⁹ In 2019, sulfur-bearing organic spacer named 2-thiophenemethyl ammonium iodide (ThMAI) was first incorporated in a 3D perovskite achieving a PCE of 21.49% with a high V_{OC} of 1.16 V. In addition, encapsulated devices showed notable stability enhancement, maintaining over 99% of initial PCE for 1680 h at ambient air conditions.¹⁰⁰ After that, several studies have been reported with thiophene-based molecules.^{101,102}

1.10 Aim of the Thesis

Herein, a fused thiophene derivative, thieno[3,2-b]thiophen-2-ylmethanaminium iodide, was successfully synthesized and employed as the large cation for surface treatment of a 3D perovskite film. Structural characterizations revealed that TTMAI forms a 2D perovskite structure $((TTMA)_2PbI_4, n = 1)$ when coated at lower

concentrations (1.5 mg/mL) and covers the surface in the salt form at higher concentrations (TTMAI-treated 3D perovskite, TT3DP). Significant PCE improvement (from 17% to over 20%) was achieved with TTMAI-treated samples, and the reason for the enhancement was shown to be related to better hole extraction properties. It was demonstrated that the capping layer significantly enhances stability even though all solar cells fabricated in this work contain a MoO_x layer. TT3DP-based PSC retained 82% of its initial PCE, while the reference solar cell maintained only 38% of it for 384 h at a relative humidity below 15%. Since we achieved exceptional stability with MoO_x-containing solar cells was achieved, fabricated ST-PSCs were also fabricated with TTMAI-treated perovskite (ST-TT3DP) with an efficiency of 17.9% PCE, one of the highest efficiencies among ST-PSCs fabricated with formamidinium methylammonium (FAMA)-based perovskites. The TTMAI treatment also enhanced the stability of ST-TT3DP significantly where after six weeks (>1000 h), the ST-TT3DP retained 87% of its initial efficiency, while the reference solar cell maintained only 69% of it. Considering the efficiency and stability aspects together, the results in this work constitute one of the best-performing ST-PSCs in the literature.

This study is reproduced from Adv. Funct. Mater. 2021, 2103130 with the permission of John Wiley & Sons, Inc.

CHAPTER 2

FABRICATION METHODS AND CHARACTERIZATION TECHNIQUES

This part of the thesis consists of three main titles: materials, fabrication procedure, and characterization techniques. The names and the brands of the chemicals used during fabrication are given under the title of materials. The second heading explains the synthesis procedure of TMMAI salt, experimental methods of nip opaque and semitransparent solar cells fabrication in detail. The last part of the chapter includes the solar cell and film characterization instruments and the analysis details.

2.1 Materials

SnO₂ colloid solution (tin (IV) oxide, 15% in H₂O colloidal dispersion) was purchased from Alfa Aesar. Formamidinium iodide (FAI) and methylammonium bromide (MABr) were purchased from Greatcell Solar, and methylammonium chloride (MACl) were purchased from Lumtec. Lead iodide (PbI₂) was purchased from Tokyo Chemical Company (TCI). Isopropyl alcohol (IPA), spiro-OMeTAD, molybdenum trioxide (MoO₃), bis(trifluoromethane), sulfonimide lithium salt (Li-TFSI), 4-tert-butyl pyridine (TBP), and chlorobenzene (CB) were provided from Sigma Aldrich. Dimethylformamide (99.9%) (DMF) and dimethyl sulfoxide (99.9%) (DMSO) were purchased from Acros Organics.

2.2 Synthesis of TTMAI and Fabrication of Opaque and Semitransparent Perovskite Solar Cells

The thieno[3,2-b]thiophen-2-ylmethanaminium iodide (TTMAI) molecule was successfully synthesized by Cevahir Ceren Akgül and the synthesis procedure was given below:

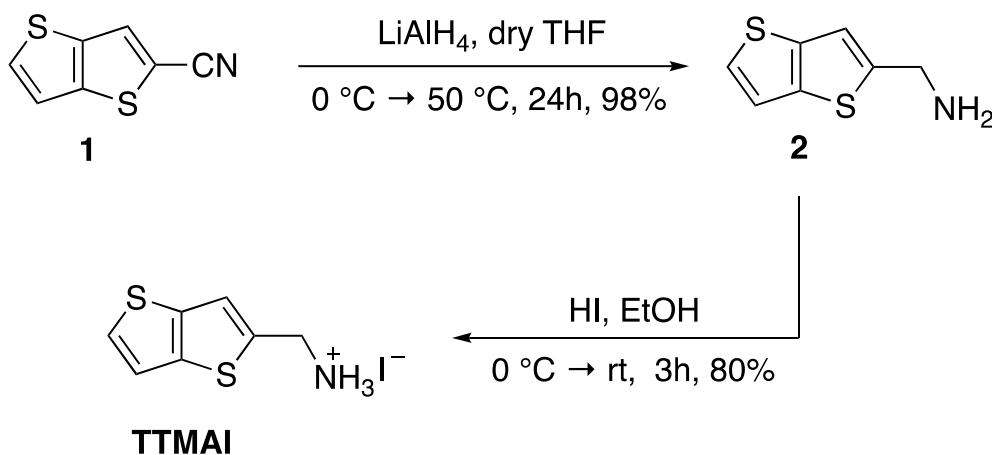


Figure 2.1. The synthesis scheme of TTMAI molecule.

Thieno[3,2-b]thiophen-2-ylmethanamine (2): The synthesis of the target compound was performed according to the literature. The commercially available thienothiophene carbonitrile (1) (0.50 g, 3.03 mmol) was dissolved in dry THF (10 mL) in a reaction flask under an argon atmosphere. In another reaction flask, LiAlH_4 (0.345 g, 9.09 mmol) was dissolved in dry THF (10 mL). The LiAlH_4 solution was added dropwise to the reaction flask containing starting material at $0\text{ }^\circ\text{C}$. After the addition, the solution was heated to $50\text{ }^\circ\text{C}$ and stirred for 24 hours. The reaction cooled down to $0\text{ }^\circ\text{C}$, and the reaction mixture was diluted with diethyl ether (10 mL). Distilled water (5 mL), 5% NaOH solution (10 mL), and MgSO_4 were added at $0\text{ }^\circ\text{C}$. The reaction was warmed to room temperature and stirred for 30 minutes. The resultant mixture was filtered and washed with diethyl ether (100 mL). The collected filtrates were concentrated under low pressure to yield the title compound as a white solid (0.503 g, 98% yield). $^1\text{H NMR}$ (400 MHz, CDCl_3) δ 7.24 (d, $J = 5.2\text{ Hz}$, 1H),

7.15 (d, $J = 5.2$ Hz, 1H), 7.03 (s, 1H), 4.04 (s, 2H) ppm. ^{13}C NMR (100 MHz, CDCl_3) δ 149.01, 137.63, 137.02, 125.08, 118.58, 114.86, 41.44 ppm.

Thieno[3,2-b]thiophen-2-ylmethanaminium iodide (TTMAI): The synthesis of the target compound was performed according to the literature with small modifications.[1] Thieno[3,2-b]thiophene-2-methylamine (2) (0.20 g, 1.18 mmol) was dissolved in ethanol (10 mL). HI (0.2 mL) was added to this solution at 0 °C, and the mixture was stirred for 3 hours. The excess solvent was evaporated under low pressure to give a dark brown solid, which was recrystallized from diethyl ether. The material was washed with excess diethyl ether and dried to give the title compound a cream-colored solid (0.16 g, 80% yield). ^1H NMR (400 MHz, DMSO-d_6) δ 8.23 (s, 3H), 7.73 (d, $J = 5.3$ Hz, 1H), 7.56 (s, 1H), 7.47 (d, $J = 5.2$ Hz, 1H), 3.37 (s, 2H). ^{13}C NMR (100 MHz, DMSO-d_6) δ 139.93, 138.36, 137.58, 129.37, 122.16, 120.39, 38.34.

The perovskite solar cells were fabricated by glass/ITO/ SnO_2 /Perovskite/Spiro-OMeTAD/ MoO_x /Au architecture, as shown in Figure 2.2. The TTMAI organic ammonium salt in IPA was coated on the 3D FAMA perovskite to form the TT3DP structure.

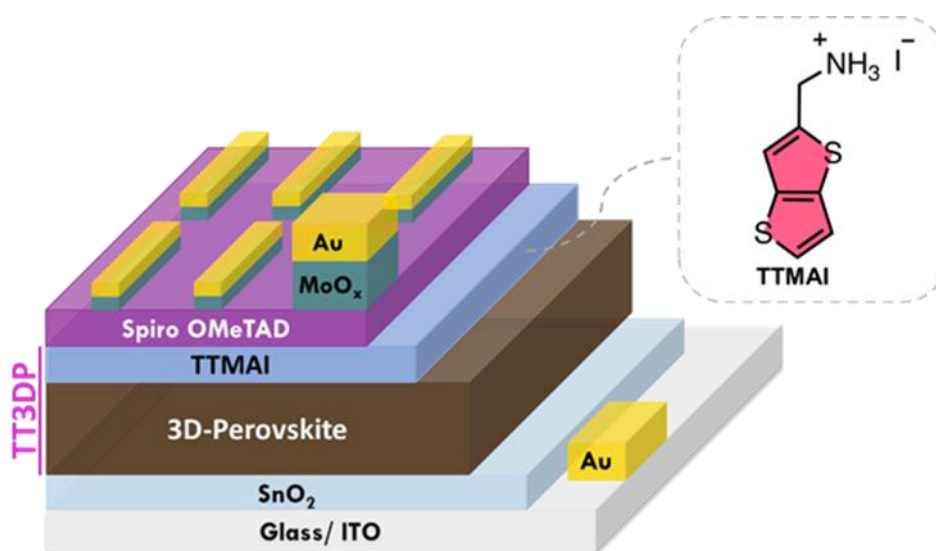


Figure 2.2. Schematics of the thieno[3,2-b]thiophen-2-ylmethanaminium iodide (TTMAI) structure and the illustration of the TT3DP solar cell architecture.

The glass substrates coated with indium tin oxide (13 ohms/sq) (ITO) were etched with zinc powder and 3 M hydrochloric acid (HCl) to create a pattern. Then, ITO samples were washed with hellmanex, DI water, acetone, and IPA for 10 min, respectively. The cleaning procedure was followed by the UV-ozone treatment of substrates for 10 min to eliminate organic residues and enhance wettability. Finally, the diluted SnO₂ solution (2.14% in deionized water) was coated on the cleaned substrates at 4000 rpm for 30 s and annealed at 150 °C for 30 min. After cooling, the samples were treated with UV-ozone for 10 min and transferred into the N₂ filled glovebox.

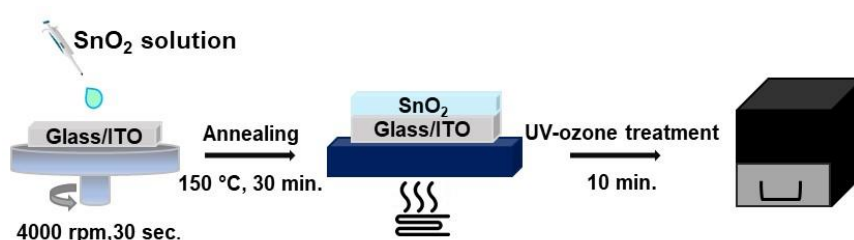


Figure 2.3. Schematic representation of the SnO₂ layer fabrication.

PbI₂ solution was prepared by dissolving 1.3 M in DMF: DMSO (95:5) (v/v) mixture. FAI: MACl: MABr (60:6:6 mg) was dissolved in 1 mL of IPA to prepare the FAMA solution. The perovskite coating was performed by a sequential method. Firstly, the PbI₂ solution was coated at 1500 rpm and annealed at 70 °C for 1 min. After cooling the substrates, the FAMA precursor solution was coated at 1500 rpm, 30 s, and annealed at 150 °C for 15 min.

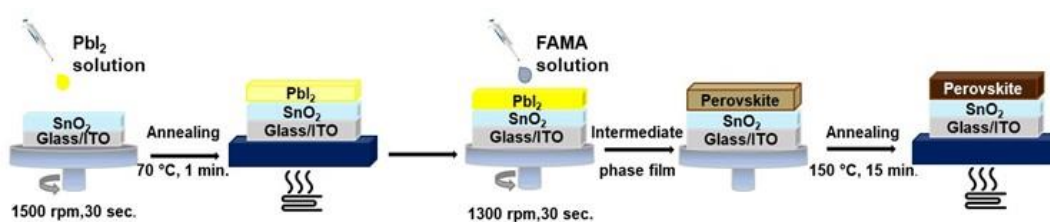


Figure 2.4. Schematic representation of the perovskite layer fabrication.

Different concentrations of TTMAI salt were dissolved in 1 mL of IPA and coated at 1000 rpm, 30 s, followed by thermal annealing at 100°C for 5 min.

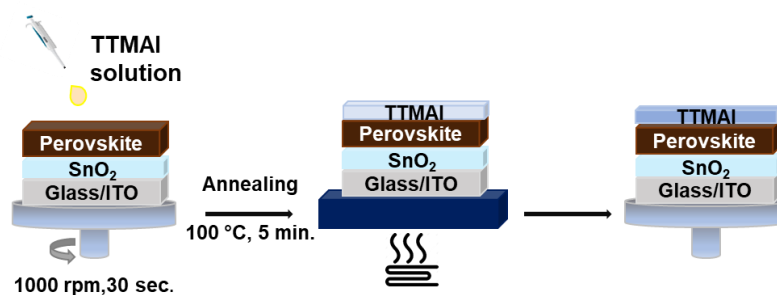


Figure 2.5. Schematic representation of the TTMAI layer fabrication.

For the preparation of the spiro-OMeTAD solution, 72.3 mg spiro-OMeTAD was dissolved in 1 mL of chlorobenzene, and 17.5 μL bis(trifluoromethane)sulfonimide lithium salt (Li-TFSI) (520 mg/mL in acetonitrile), 28.8 μL 4-tert-butylpyridine (TBP) was added in it as the dopants. The coating was carried out at 3000 rpm, 20 s. Finally, 20 nm MoO_3 and 60 nm gold were evaporated on the substrates under a high vacuum consecutively.

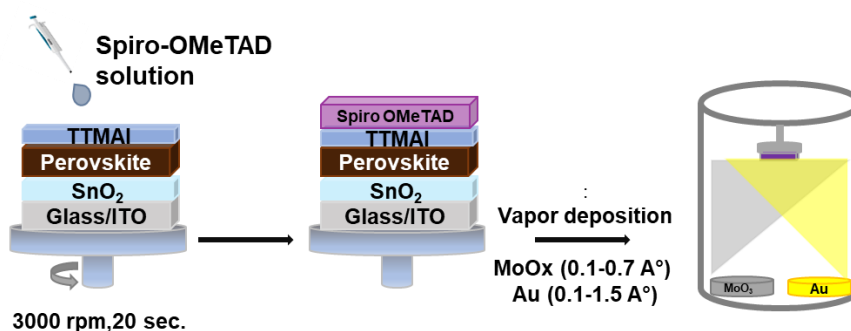


Figure 2.6. Schematic representation of the Spiro-OMeTAD, MoO_x , and Au layer deposition.

Fabrication of the ST-PSCs was identical to those of opaque solar cells up to the back-contact deposition. ITO bottom electrode was deposited by magnetron sputtering, which was carried out at a power density of 2.2 W.cm^{-2} with a deposition pressure of 2 mTorr. Lastly, to lower the sheet resistance of ITO film (30 ohms/sq), 60 nm of the current-collecting gold film was deposited by thermal evaporation.

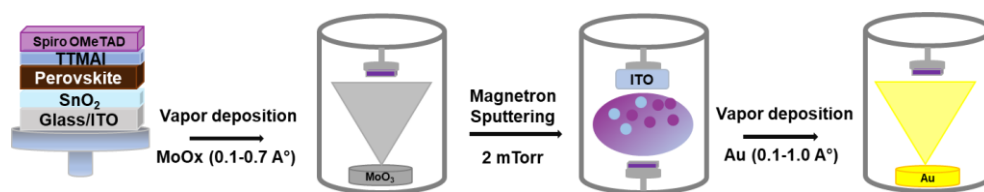


Figure 2.7. Schematic representation of the ST-PSC fabrication.

Solution for 2D perovskite ($n = 1$) film was prepared by dissolving TTMAI and PbI₂ (2:1) in the DMF:DMSO (95:5) (v:v) mixture. The precursor solution was coated at 3000 rpm, 30 s, and annealed at 100 °C for 10 min. Precursor solutions for FA and/or MABr incorporated quasi-2D perovskites were prepared by dissolving TTMAI, MAI, PbI₂ (2:1:2), TTMAI, FAI, PbI₂ (2:1:2), TTMAI, MABr, PbI₂ (2:1:2), and TTMAI:MABr:FAI: PbI₂ (2:0.5:0.5:2) in DMF:DMSO (95:5) (v:v) mixture. All solutions were coated at 3000 rpm, 30 s, followed by thermal annealing at 100 °C for 10 min.

2.3 Device Characterizations

This section explains the characterization techniques and their processes used to analyze 3D and TT3DP perovskite solar cells.

2.3.1 Current Density-Voltage (J-V)

The J-V measurements were performed by Keithley 2400 source meter, and Pico G2V LED solar simulator under AM 1.5G with 100 mW/cm² illumination intensity with a scan rate of 100 mV/s. The active areas of metal contacts were determined as 3 mm² for the opaque cells and 3.14 mm² for semitransparent cells using polycrystalline silicon shadow masks. The solar cells used in the stability test are kept in the dark environment at 15% relative oxygen, while they are not measured. The device measurements were carried out under the same conditions for all solar cells.

2.3.2 External quantum efficiency (EQE)

The external quantum efficiency is defined as the ratio of the number of collected carriers by solar cells to the number of incident photons. The spectral response (SR), which is the proportion of current generated to the incident power, is critical to measuring EQE.¹⁰³ The equation below defines the relationship between EQE and SR:

$$EQE(\lambda) = \frac{hc}{q\lambda} \times SR \quad (2.3)$$

h is a Plank constant (6.63×10^{-34} J.s), c is the speed of light (3.0×10^8 m/s), q is the electronic charge, and λ is a wavelength.

The measured EQE at a specific wavelength is used for the calculation of integrated J_{sc} . The following equation calculated the integrated Jsc values:

$$J_{sc} = \int qEQE(\lambda)S(\lambda)d\lambda \quad (2.4)$$

q is referred to as elementary charge, and $S(\lambda)$ is a photon flux.

The EQE measurement was conducted by a PV characterization system (Bentham Instruments, PVE300) equipped with a light source and monochromator to calculate integrated Jsc values of the reference and TTMAI-treated solar cells.

2.3.3 Impedance Spectroscopy

Impedance measurements were performed using MFIA Impedance Analyzer (Zurich Instruments) in the frequency range between 10 Hz to 1 MHz with an oscillation peak amplitude of 15 mV. The cell was operated under the operation (open-circuit) condition at all times using a DC blocking capacitor connected to the signal output

of the impedance analyzer while the true oscillation voltage across the cell was sensed via 4-terminal (4T) measurement mode and illuminated with light-emitting diode (LED), ($\lambda=625$ nm) (Thorlabs M625L4), which was calibrated by the short-circuit photocurrent of a sample cell, corresponding to an equivalent of 0.1 Suns AM 1.5G.

2.4 Film Characterizations

This section explains the characterization techniques used to analyze perovskite film surfaces with and without TTMAI insertion.

2.4.1 Grazing Incidence X-Ray Diffraction (GIXRD)

Grazing Incidence X-ray Diffraction (GIXRD) measurements were conducted to distinguish the difference in the crystal structure of the reference and the TTMAI treated films. The GIXRD patterns were obtained (Rigaku Ultima-IV X-Ray diffractometer) with Cu K α radiation at 30 kV and 40 mA operation conditions and a grazing angle of 0.5 ° at a scan rate of 2 °/min. The Crystallite size of the grains is determined by the Debye-Scherrer Equation, where D represents the crystallite size, K is the crystallite shape factor (generally accounted as 0.9), λ is referred to the wavelength of the X-ray, β represent the full-width at half-maximum of the X-ray diffraction peak, and θ is a Bragg angle.¹⁰⁴

$$D = \frac{K\lambda}{\beta \cos\theta} \quad (2.1)$$

2.4.2 Scanning Electron Microscopy (SEM)

Scanning Electron Microscopy (SEM) measurements were performed to observe the change in surface morphology of the reference film upon TTMAI insertion and operated at 30.00 kV with a resolution of 1.2 nm (QUANTA 400F Field Emission).

2.4.3 Atomic Force Microscopy (AFM)

Atomic Force Microscopy (AFM) analysis was carried out to observe an alteration in the surface roughness (Park System, PSIA, XE100).

2.4.4 Absorbance

Reflection (R), transmission (T), and external quantum efficiency (EQE) measurements were performed by a PV characterization system equipped with a BaSO₄ covered integrating sphere (Bentham Instruments, PVE300) in the range of 300-850 nm. Absorption (A) of the films was then calculated by the formula below:

$$A = 1 - R - T \quad (2.2)$$

2.4.5 Photoluminescence (PL)

The reference and TT3DP films were coated on glass substrates for the photoluminescence spectroscopy measurements (Horiba Jobin Yvon, Fluorolog 3). The films were excited from the glass sides of the samples with an excitation wavelength of 495 nm. Analysis was performed to determine the effect of TTMAI salt on defect passivation and charge transportation.

2.4.6 X-Ray Photoelectron Spectroscopy (XPS) and Angle-Resolved XPS (ARXPS)

X-ray photoelectron spectroscopy (XPS), angle-resolved XPS (ARXPS), and Ultraviolet Photoelectron Spectroscopy (UPS) experiments were carried out (Physical Electronics (PHI), VersaProbe 5000) under high vacuum with a base pressure of 1×10^{-9} mbar. X-ray energy of 23.4 W, pass energy of 58.70 eV, energy step of 0.1 eV, and X-ray spot size of 100 μm were used for all three angles (20, 45, 70°) for the ARXPS measurement.

2.4.7 Ultraviolet Photoelectron Spectrophotometry

The He-I discharge lamp (21.22 eV) was used as the light source in UPS measurements. The positions of the valence band maxima were determined using linear extrapolation of the leading edge of the valence band emissions, and work function was determined from the linear extrapolation with the baseline of the secondary electron onset.

2.4.8 Contact Angle

Contact angle measurements were conducted to observe the effect of TTMAI salt on hydrophobicity (the Attension Theta Lite), and water was used as the solvent.

CHAPTER 3

RESULTS AND DISCUSSION

In the first part of this chapter, photovoltaic characterization of the spin speed optimization of TTMAI was demonstrated. In the second part of the study, the influence of TTMAI concentration on device performance and surface change was investigated, and this part was divided into two subcategories. In the first sub-title, several photovoltaic characterizations, including J-V and EQE, were studied for all concentrations of the TTMAI. The hysteresis, reproducibility, and IS analyses were examined for the best-performing TTMAI concentration cells and the reference cell. In the second sub-title, the change in surface morphology caused by different TTMAI concentrations on the 3D FAMA perovskite surface was examined using GIXRD, XPS, ARXPS, SEM, AFM, PL, and absorbance characterization techniques, respectively. In addition to the characterization of opaque solar cells, the photovoltaic analysis of the semitransparent solar cells was also accomplished. The final title of the chapter explains the influence of TTMAI on the stability of both opaque and ST-PSCs.

3.1 Spin rate optimization of the TTMAI ammonium salt

The TTMAI organic compound is coated at different spin rates to determine optimized spin speed. The reference and TT3DP solar cells' statistical distribution graphs were given in Figure 3.1, and detailed device parameters were interpreted in Table 3.1. TTMAI-treated solar cells coated at 1000 rpm showed superior device performance due to a significant enhancement of FF. The average PCE was obtained as 16.03% for reference and 18.00% for the TT3DP (1000 rpm) solar cells.

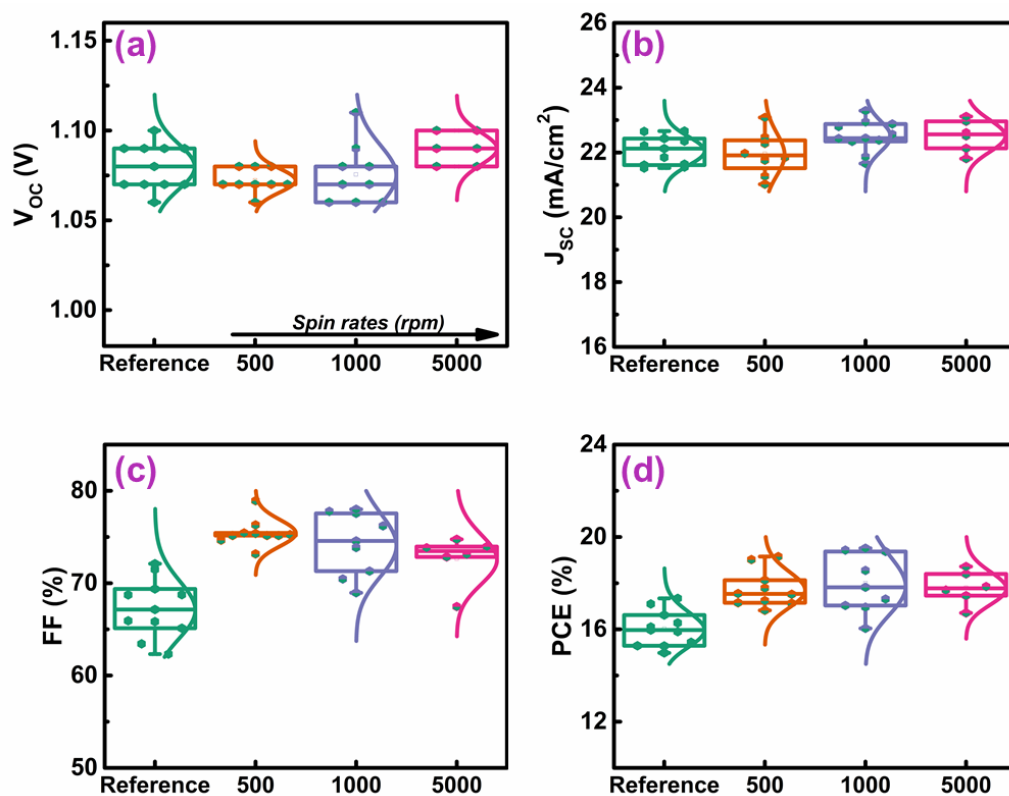


Figure 3.1. (a) V_{oc} , (b) J_{sc} , (c) FF, and (d) PCE statistics of reference solar cells and solar cells treated with different spin speeds of TTMAl.

Table 3.1 Average and the highest device parameters of the reference and TTMAl-treated solar cells

| Devices | | V_{oc} (V) | J_{sc} (mA/cm ²) | FF (%) | PCE % |
|------------------------|---------|-----------------|--------------------------------|------------------|------------------|
| Reference | Average | 1.08 ± 0.01 | 22.05 ± 0.44 | 67.30 ± 3.12 | 16.03 ± 0.77 |
| | Highest | 1.07 | 22.65 | 71.48 | 17.34 |
| TTMAl, 500 rpm | Average | 1.07 ± 0.01 | 21.96 ± 0.66 | 75.46 ± 1.45 | 17.75 ± 0.79 |
| | Highest | 1.08 | 22.47 | 78.92 | 19.15 |
| TTMAl, 1000 rpm | Average | 1.08 ± 0.02 | 22.51 ± 0.47 | 74.29 ± 3.40 | 18.00 ± 1.27 |
| | Highest | 1.08 | 23.29 | 77.55 | 19.51 |
| TTMAl, 5000 rpm | Average | 1.09 ± 0.01 | 22.52 ± 0.49 | 72.66 ± 2.63 | 17.81 ± 0.71 |
| | Highest | 1.10 | 23.11 | 73.83 | 18.72 |

In addition, the highest efficiency of TT3DP and reference PSCs were obtained as 19.51% ($V_{OC} = 1.08$ V, $J_{SC} = 23.29$ mA/cm², FF = 77.55%) and 17.34% ($V_{OC} = 1.07$ V, $J_{SC} = 22.65$ mA/cm², FF = 71.48%), respectively (Figure 3.2).

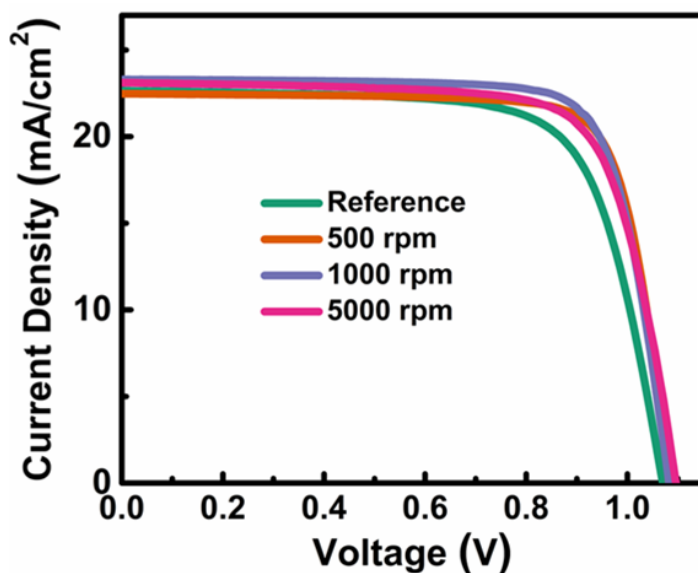


Figure 3.2. J-V curves of the best-performing reference and TT3DP PSCs.

The integrated J_{sc} results calculated from the EQE measurements for the reference and TTMAI solar cells coated at different spin speeds were 22.04 mA/cm², 21.97 mA/cm², 22.34 mA/cm² and 22.06 mA/cm², respectively. (Figure 3.3).

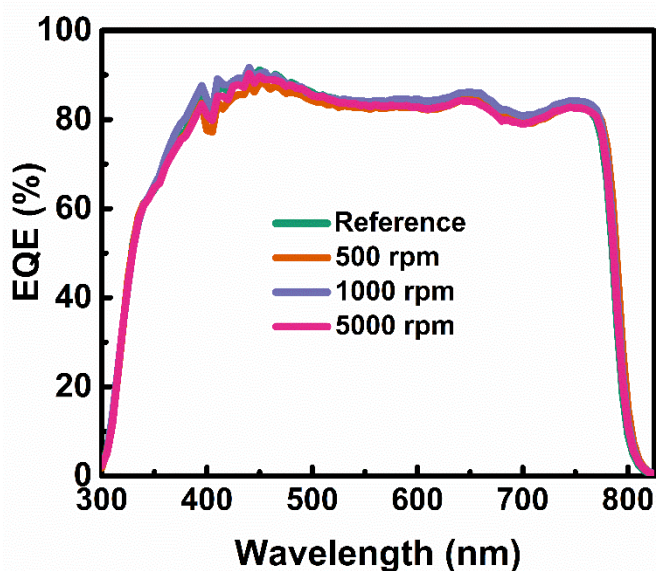


Figure 3.3. EQE graphs of the best-performing solar cells.

3.2 Concentration Optimization of TTMAI salt

The 3D perovskite films were treated with four different concentrations (1.5, 2.0, 2.5, and 3.0 mg/mL) of TTMAI organic salt to optimize the TTMAI layer further. The influence of the TTMAI was investigated under the photovoltaic and surface characterizations sections.

3.2.1 Photovoltaic Characterization of the Reference and TT3DP PSCs

It has been shown that the fill factor was improved significantly in addition to slight enhancements in V_{oc} and J_{sc} with increased TTMAI concentration, as shown in Figure 3.4.

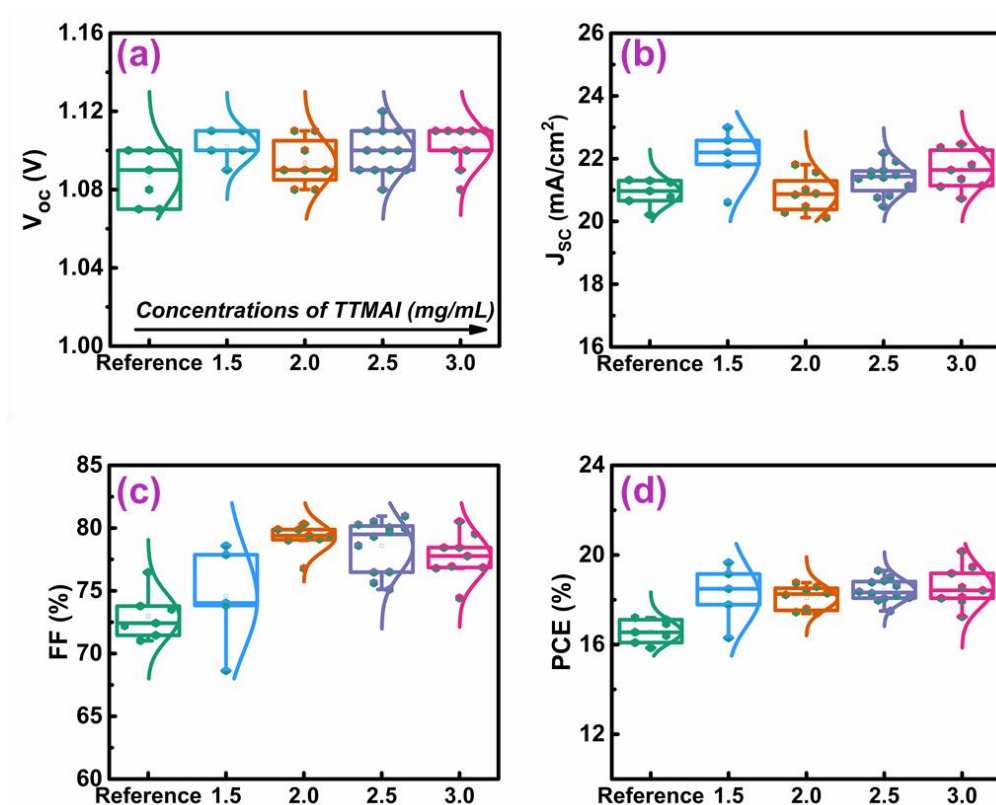


Figure 3.4. (a) V_{OC} , (b) J_{SC} , (c) FF and (d) PCE statistics of reference solar cells and solar cells treated with different concentrations of TTMAI.

Table 3.2 Average and the highest device parameters of the reference and TTMAI-treated solar cells

| Devices | | V_{OC} (V) | J_{SC} (mA/cm ²) | FF (%) | PCE % |
|-------------------------|---------|--------------|--------------------------------|--------------|--------------|
| Reference | Average | 1.09 ± 0.01 | 20.93 ± 0.41 | 72.98 ± 1.83 | 16.59 ± 0.51 |
| | Highest | 1.09 | 21.30 | 73.78 | 17.11 |
| TTMAI, 1.5 mg/mL | Average | 1.10 ± 0.01 | 22.04 ± 0.91 | 74.59 ± 3.97 | 18.27 ± 1.31 |
| | Highest | 1.10 | 23.01 | 76.08 | 19.66 |
| TTMAI, 2.0 mg/mL | Average | 1.09 ± 0.01 | 20.88 ± 0.59 | 79.23 ± 1.08 | 18.09 ± 0.53 |
| | Highest | 1.09 | 21.57 | 77.87 | 18.58 |
| TTMAI, 2.5 mg/mL | Average | 1.10 ± 0.01 | 21.35 ± 0.49 | 78.59 ± 2.08 | 18.42 ± 0.51 |
| | Highest | 1.10 | 21.91 | 80.27 | 19.30 |
| TTMAI, 3.0 mg/mL | Average | 1.10 ± 0.01 | 21.65 ± 0.62 | 77.75 ± 1.77 | 18.57 ± 0.89 |
| | Highest | 1.11 | 22.47 | 80.52 | 20.16 |

The highest PCE of TT3DP and reference PSCs were obtained as 20.16% (V_{OC} = 1.11 V, J_{SC} = 22.47 mA/cm², FF = 80.52%) and 17.11% (V_{OC} = 1.09 V, J_{SC} = 21.30 mA/cm², FF = 73.78%), respectively (Figure 3.5). Although the treatment with 3.0 mg/mL TTMAI concentration resulted in the highest average PCE (Figure 3.4), a turbid solution was attained at this concentration compared to others (Figure 3.6). Therefore, all studies were conducted with 2.5 mg/mL concentration, in which the highest PCE was achieved as 19.30% (V_{OC} = 1.10V, J_{SC} = 21.91 mA/cm², FF = 80.27%).

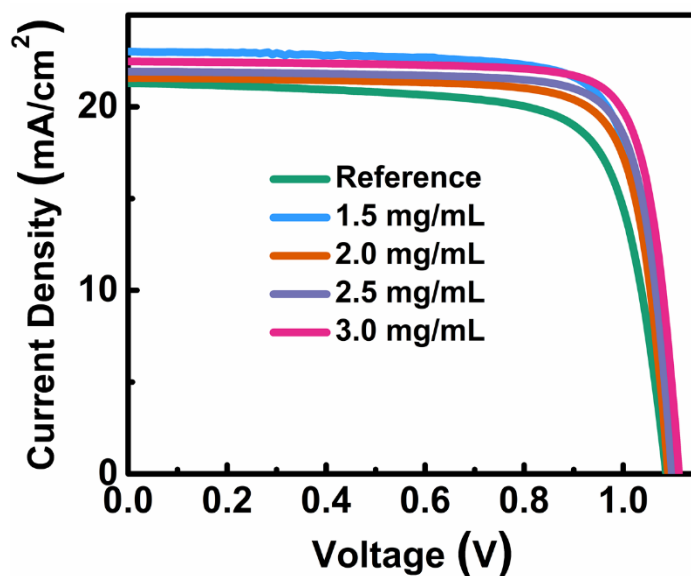


Figure 3.5. J-V curves of the best-performing PSCs.



Figure 3.6. Images of the solutions of TTMAI in IPA with different concentrations (From left to right: 3.0 mg/mL, 2.5 mg/mL, and 2.0 mg/mL).

The EQE spectra of the best-performing solar cells were given in Figure 3.3. The integrated J_{sc} results were calculated for the reference, and TTMAI treated solar cells as 22.01 mA/cm², 22.25 mA/cm², 21.81 mA/cm², 21.86 mA/cm², and 21.83 mA/cm², respectively, and they are consistent with those obtained from the J-V measurements.

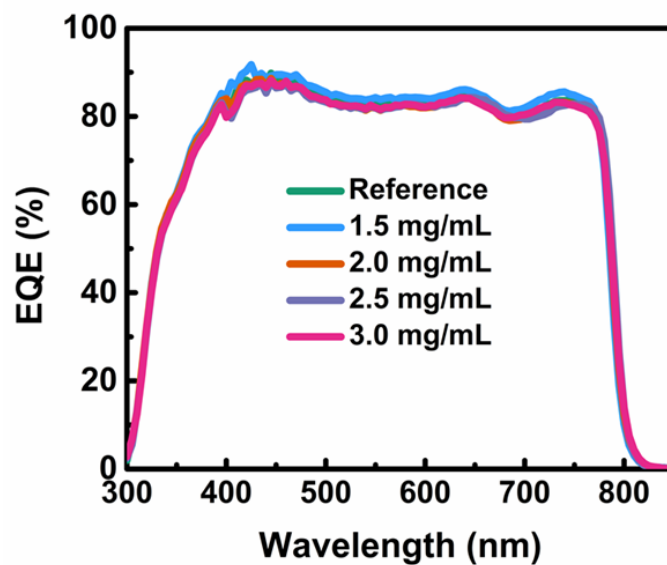


Figure 3.7. EQE spectra of the best performing solar cells.

Reproducibility is one of the critical factors for the realization of perovskite solar cells. To ensure repeatability, histograms containing the device parameters of many solar cells produced under the same conditions should show narrow efficiency fluctuation statistics from batch to batch and device to device.¹⁰⁵ As seen in Figure 3.8, a high reproducibility was obtained for all reference and TT3DP PSCs (over 20 devices).

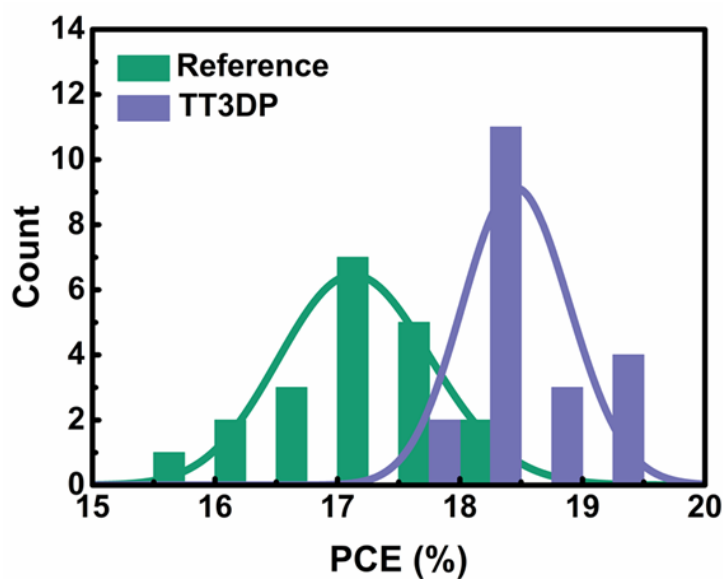


Figure 3.8. Histogram of reference and TT3DP perovskite solar cells, out of 20 devices.

The hysteresis has resulted from the ion migration or accumulation in the interfaces. It has been revealed that scan rate and bias voltage have an essential impact on the hysteresis behavior of the solar cells.¹⁰⁶ The effect of TTMAI on suppressing ion migration at different scan rates has been investigated in Figure 3.9. Hysteresis measurements were performed by scanning the corresponding solar cells in both directions (reverse and forward) three times at the same speed, and the hysteresis index (HI) results were calculated with the following formula:

$$HI = \frac{PCE_{RS} - PCE_{FS}}{PCE_{RS}} \quad (3.1)$$

In which RS is referred to reverse scan, and FS is referred to forward scan measurements. Absolute values of HI results were taken, mean and standard deviation values were calculated accordingly. It can be seen in Table 3.3 and Figure 3.9 that hysteresis decreased significantly at low scan rates in TTMAI-treated cells compared to reference cells. It should be highlighted that TT3DP PSC has a lower hysteresis index than reference PSCs revealing that insertion of a TTMAI layer enhances hole extraction and reduces capacitive charge accumulation.

Table 3.3 Hysteresis Index (%) calculations of the reference and the champion TT3DP perovskite solar cells at different scan rates.

| Devices / Scan Rates (mV/s) | 400 | 200 | 40 | 13 |
|------------------------------------|--------------|-------------|-------------|-------------|
| Reference | 10.03 ± 2.53 | 2.89 ± 2.97 | 2.50 ± 1.44 | 5.59 ± 3.54 |
| TT3DP | 6.73 ± 5.42 | 3.17 ± 0.33 | 2.44 ± 0.78 | 1.81 ± 1.04 |

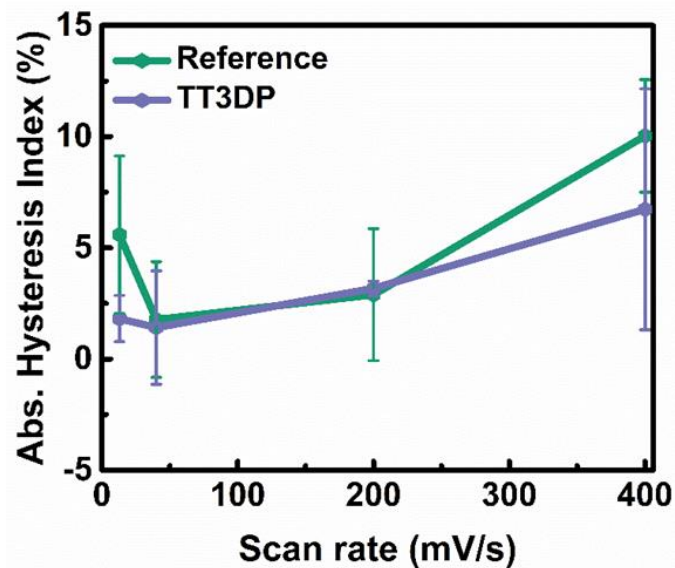


Figure 3.9. Absolute hysteresis index graph of the reference and the TT3DP solar cells at different scan rates.

The impedance spectra of reference and TT3DP solar cells are displayed via Nyquist plots, as shown in Figure 3.10. The measurements were performed under the illumination of 0.1 suns and working (open-circuit) conditions. Under operating conditions, carrier generation is fully compensated by recombination, and there is no net charge carrier transport between the perovskite stack and interfaces. Thus, the resulting high-frequency impedance response can be easily analyzed by correlating it with the recombination process. The high-frequency semi-circle is generally attributed to a geometrical capacitance or recombination resistance¹⁰⁷. In this regard, the shrinkage of the high-frequency semi-circle upon insertion of the TTMAI layer, compared to the reference cell, indicates faster recombination since the recombination resistance decreased.

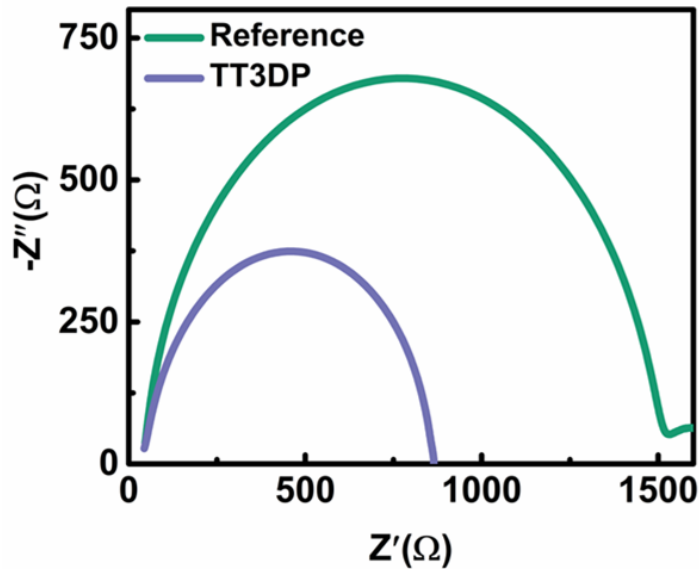


Figure 3.10. Nyquist plot of the reference and TT3DP PSCs.

3.2.2 Surface characterization of the reference and TT3DP films

The GIXRD measurements for both reference and TTMAI treated films were conducted with a grazing angle of 0.5° . The new peak formation at a low angle (5.10°) was observed in the GIXRD pattern of the TT3DP film, and a peak below 10° is commonly attributed to the formation of a low dimensional perovskite layer.¹⁰⁸⁻¹¹¹ The observed peak was initially assigned to 2D perovskite ($n=1$) with a general formula of $\text{TTMA}_2\text{PbI}_4$, and based on this opinion, pure 2D perovskite ($n=1$) film was formed on SnO_2 , and GIXRD analysis was performed, which revealed a peak at 5.60° (Figure 3.11). Due to the considerable variation in the GIXRD peak, a pure 2D perovskite formation was excluded.

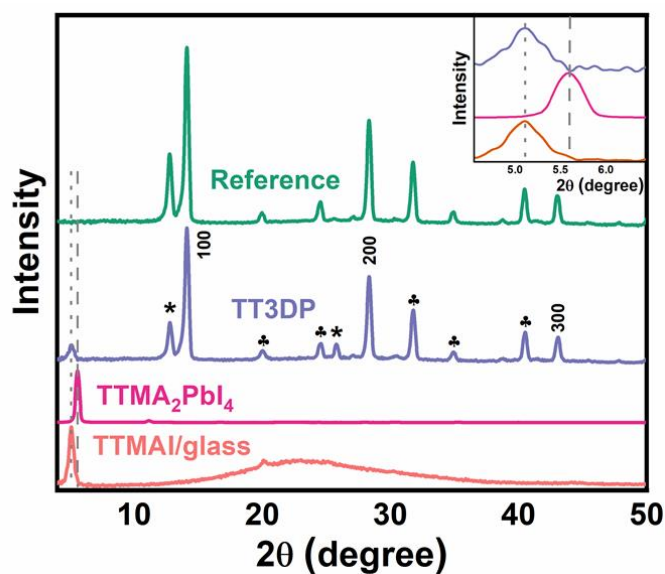


Figure 3.11. GIXRD pattern of the reference 3D perovskite, TTMAI-coated glass, $\text{TTMA}_2\text{PbI}_4$, and perovskite treated with TTMAI (TT3DP). * and ♣ represent diffraction peaks of PbI_2 and 3D perovskite, respectively. The dotted and dashed lines represent the diffraction peak of TTMAI and $\text{TTMA}_2\text{PbI}_4$ below 10° , respectively.

Next, several thin films were prepared from precursor solutions of TTMAI, MAI, and PbI_2 (2:1:2) and TTMAI, MABr, FAI, and PbI_2 (Figure 3.12) on SnO_2 to address the possible formation of quasi-2D perovskites with or without incorporation of Br^- and FA^+ ions. Yet, none of these films displayed a GIXRD peak around 5.10° . Finally, GIXRD for the TTMAI coated glass was carried out, and a diffraction peak at 5.10° was observed, which is consistent with the GIXRD peak of the TT3DP layer below 10° (Figure 3.11).

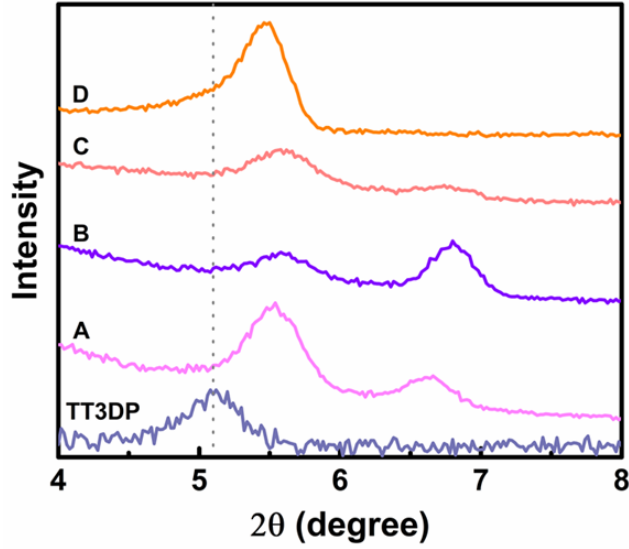


Figure 3.12. GIXRD patterns of quasi 2D perovskite films prepared from solutions **A** (TTMAI, MAI, PbI_2 | 2:1:2), **B** (TTMAI, MABr, PbI_2 | 2:1:2) **C** (TTMAI, MABr, FAI, PbI_2 | 2:0.5:0.5:2) and **D** (TTMAI, FAI, PbI_2 | 2:1:2) letters denote the various composition the of perovskites. The dotted line represents the position of the diffraction peak of TTMAI on the 3D perovskite (**TT3DP**).

In addition, compared to the 3D perovskite film, almost no change was observed in the full width half maximum (FWHM) and the crystallite size (D) of the $\langle 100 \rangle$ -oriented perovskite peak for TT3DP, indicating that TTMAI did not incorporate into the 3D bulk (Table 3.4).

Table 3.4 full width at half maximum (FWHM), and crystallite size parameters obtained from the GIXRD measurements for the reference and TT3DP films

| <i>Samples</i> | <i>FWHM of the $\langle 100 \rangle$ 3D-perovskite ($^\circ$)</i> | <i>Crystallite Size 3D-Perovskite (nm)</i> |
|----------------|---|--|
| Reference | 0.344 | 24.3 |
| TT3DP | 0.353 | 23.7 |

Another GIXRD study was performed to see the effect of TTMAI concentration on the surface of the 3D perovskite film. The GIXRD patterns showed a diffraction peak at 5.60° was observed for TTMAI with a 1.5 mg/mL concentration. (Figure 3.13), consistent with the pure low dimensional perovskite structure (5.60°) as shown in Figure 3.11. However, this peak shifts to the lower angle (5.10°) as the concentration of TTMAI increases, which correlates with the TTMAI diffraction peak at 5.10° (Figure 3.13). The curious observation of the 2D perovskite peak disappearance at higher TTMAI concentrations stays unresolved at the moment and will be investigated in detail.

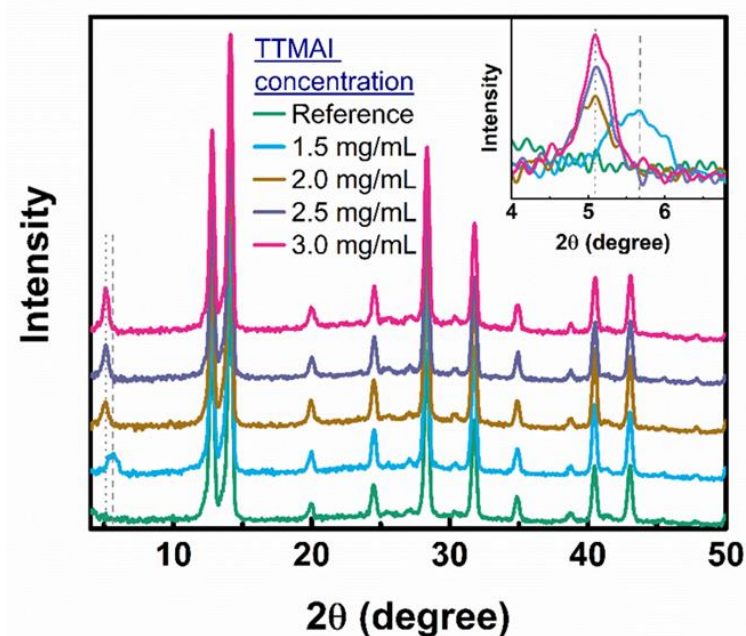


Figure 3.13. GIXRD patterns of 3D perovskite film treated with different concentrations of TTMAI.

The X-ray Photoelectron Spectroscopy (XPS) technique is generally used to analyze the surface chemistry of the compounds. The XPS measurements were conducted to confirm the existence of the organic capping layer on the 3D film. Unlike the reference perovskite composition, the TTMAI structure contains a sulfur element(S). The analysis result showed that TTMAI- treated perovskite surface has an S 2s signal, indicating an ammonium salt layer formation (Figure 3.14).

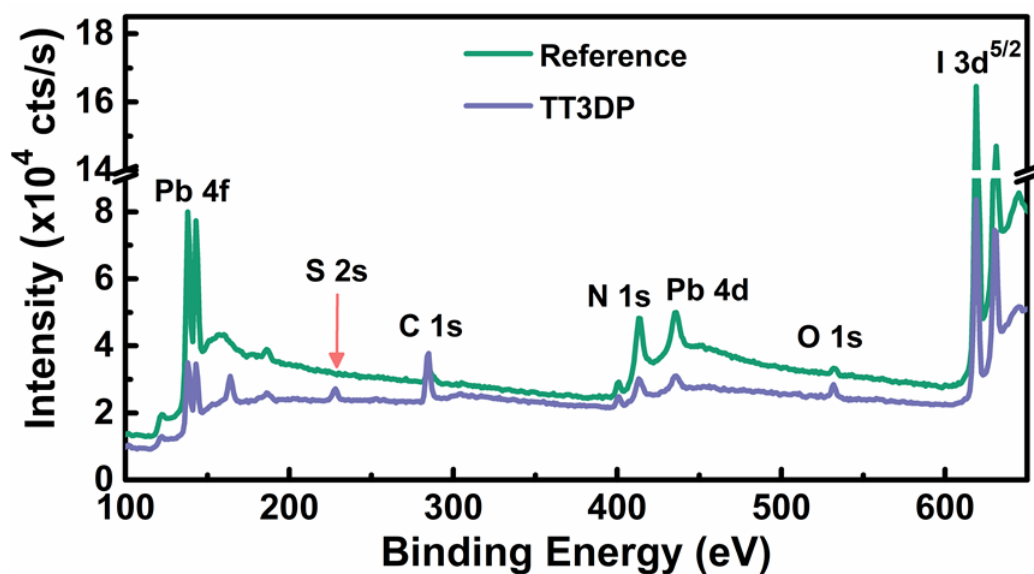


Figure 3.14. XPS spectra of the reference and TT3DP films.

Moreover, angle-resolved X-ray photon spectroscopy (ARXPS) performed at 20, 45, and 70° displayed that S 2s peak position does not change with take-off angle, indicating the oxidation state of the sulfur is uniform near the surface (up to about 8 nm). Additionally, no metallic Pb was found on the perovskite surface, revealing that the analyses were completed without degradation of the samples (Figure 3.15).

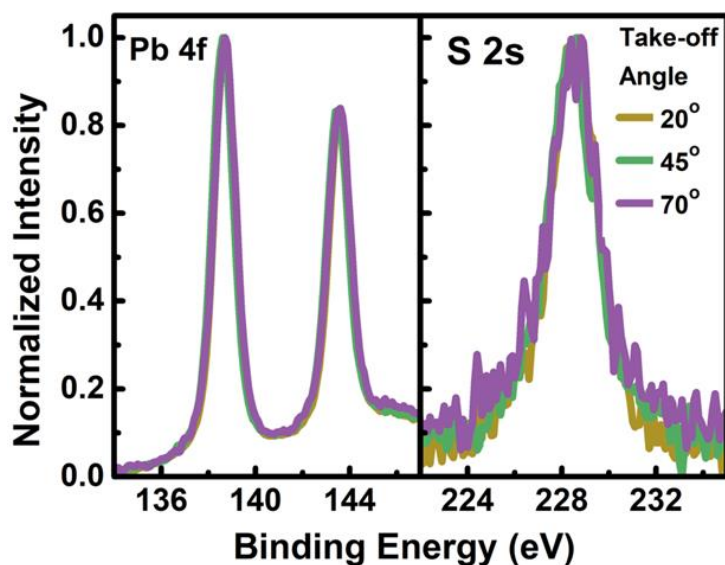


Figure 3.15. Normalized ARXPS spectra for Pb 4f and S 2s signals of the TT3DP film taking different take-off angles.

Scanning electron microscopy (SEM) was conducted to observe the change in the 3D perovskite surface upon TTMAI addition. The top view images revealed that the surface morphology of the 3D film (i.e., grain boundaries have mostly vanished.) had changed significantly after treatment with TTMAI (Figure 3.16), and this change became more pronounced with increasing TTMAI concentration. In addition to the TTMAI salt concentration, the impact of the solvent (IPA) on the surface morphology was investigated and it was observed that there was no significant alteration in the reference film surface.

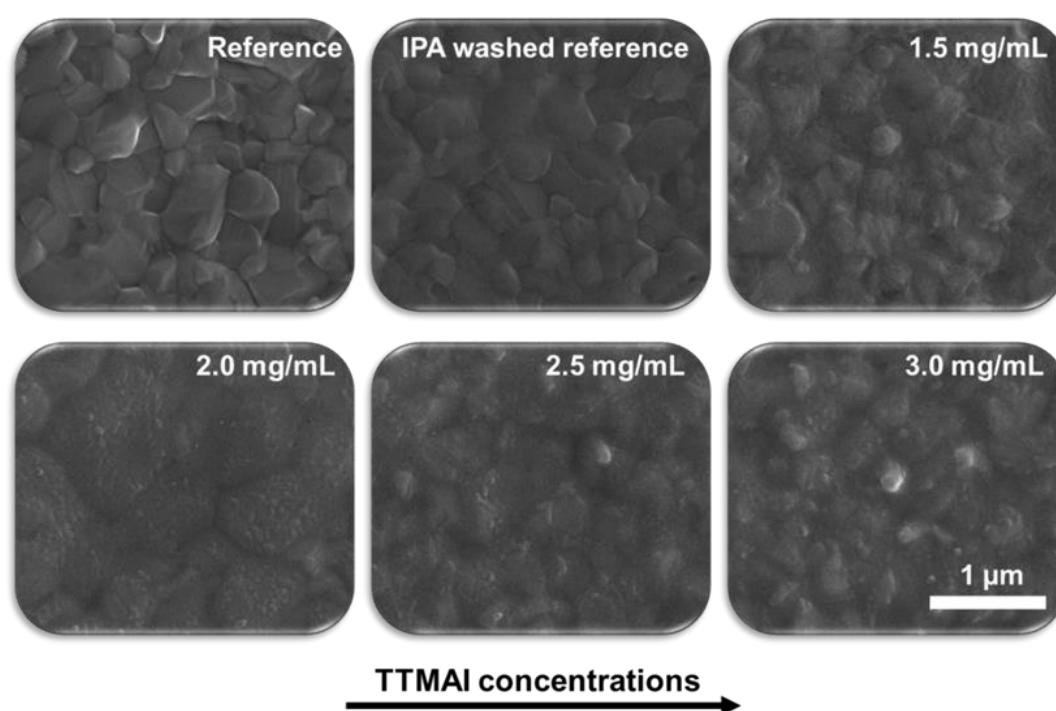


Figure 3.16. Top-view SEM images of the reference, IPA washed reference and TTMAI (with different concentrations) films.

In addition, AFM analysis was performed to observe roughness change with the TTMAI layer insertion. The TTMAI treatment slightly reduced the roughness of the 3D film surface, which is consistent with the SEM images. The root square means values were calculated as 27.6 ± 3.21 and 26.6 ± 2.43 nm for the reference and TT3DP films, respectively. (Figure 3.17).

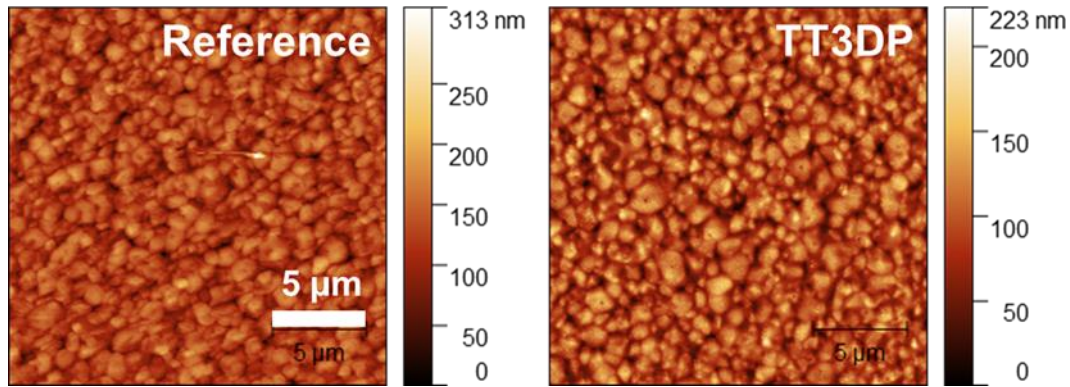


Figure 3.17. AFM topography images of the reference and TT3DP films.

The absorbance spectra of the reference and TT3DP films are depicted in Figure 3.18. Measurements showed that the TMAI surface treatment had no significant effect on the absorption peak intensity of the reference perovskite and revealed that the modification with TMAI did not cause an increase in J_{SC} in agreement with the J-V measurement results of the solar cells.

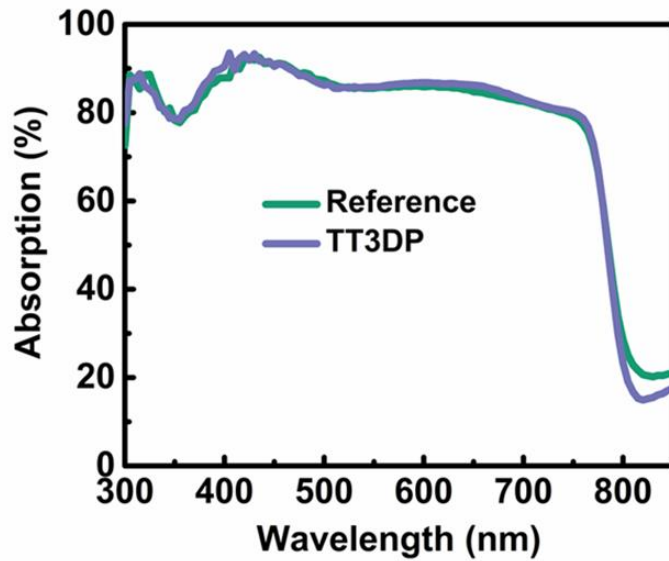


Figure 3.18. Absorption spectra of the reference and TT3DP films.

The PL spectroscopy of reference and TT3DP films were performed to observe the nonradiative recombination process and surface recombination velocity changes through modification with the TMAI. A significant decrease in PL intensity was

observed upon TTMAI addition (Figure 3.19). The measurement results showed that, unlike common interface modifiers, TTMAI salt neither reduced trap densities nor surface recombination as there is only a slight increase in V_{OC} . It can be concluded that ammonium salt did not passivate ionic defects on the 3D surface and increased surface recombination velocity, which is consistent with the IS results. As a result, in the absence of notable J_{SC} and V_{OC} increase, it was associated that the PL quenching observed in the TT3DP PSCs with better hole transport, coherent with the significantly enhanced fill factors, shown in Figure 3.5.

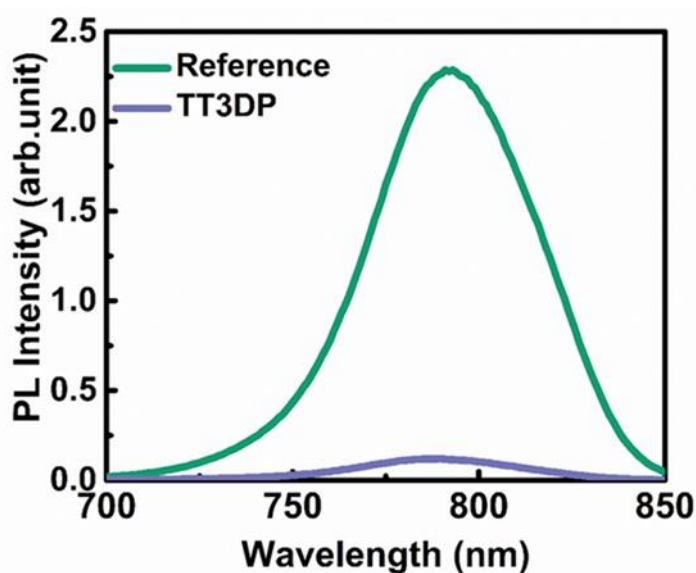


Figure 3.19. PL spectra of the reference and TT3DP films.

The UPS measurement was carried out for TTMAI salt coated on ITO substrate to determine the work function (Φ) and valance band maximum energy levels. The radiation was generated by a Helium discharge lamp (21.22 eV), and a bias of 7 eV was applied. The secondary electron cut-off energy ($E_{cut-off}$) is the low kinetic energy onset of the spectrum. The work function is calculated by subtracting $E_{cut-off}$ from photon energy (21.22 eV) (Equation 3.2).

$$\phi = h\nu - E_{cut-off} \quad (3.2)$$

The ionization energy was determined by Equation 3.3.

$$IE = \phi + (E_{VBM} - E_F) \quad (3.3)$$

In which IE represents ionization energy, E_F is Fermi level energy, and E_{VBM} is the valance band energy, respectively. The ionization energy of the TTMAI film was calculated as-5.36 eV (Figure 3.20).

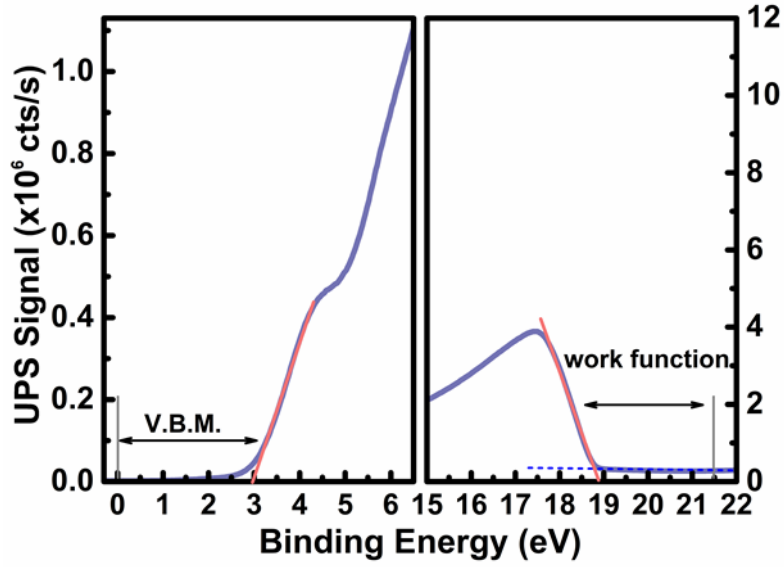


Figure 3.20. UPS spectra of the TTMAI film and linear fits to determine the work function and VBM.

An illustration of the energy band diagram of ITO, 3D perovskite, TTMAI, Spiro-OMeTAD, and Au is demonstrated in Figure 3.21. The band energy alignment clearly showed that TTMAI is favorably lying between the perovskite and hole transport layer.

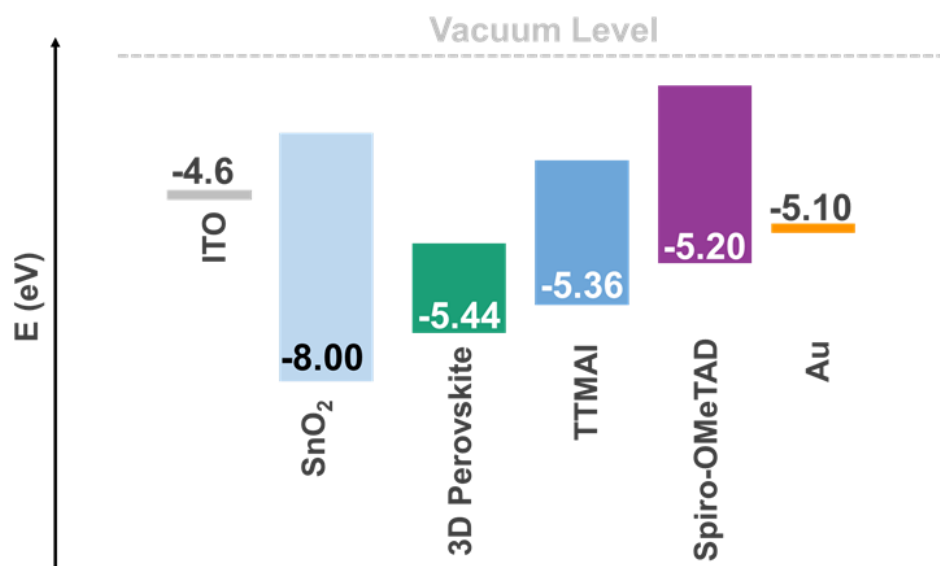


Figure 3.21. Schematic representation of the band-energy diagram of TT3DP perovskite solar cells.

The contact angle measurement was performed to clarify the influence of TTMAI salt on the hydrophobicity of the 3D FAMA perovskite. As seen in Figure 3.22, a promising increase at the angle was observed for TT3DP films due to the hydrophobic nature of the ammonium salt.



Figure 3.22. Contact angle images of the reference and TT3DP films.

3.3 Characterizations of the Semitransparent PSCs

The semitransparent solar cells were fabricated by glass/ITO/SnO₂/Perovskite/Spiro-OMeTAD/MoO_x/ITO/Au architecture. The ITO layer fabrication process was carried out via magnetron sputtering, and the MoO_x layer was used for providing a buffer layer between HTL and TCO. The ST-PSCs were demonstrated for both reference and best-performing TTMAI concentration. The results clearly showed that all device parameters improved significantly by inserting the TTMAI organic layer, as shown in Figure 3.23. The highest PCE for the reference solar cells was obtained as 16.16% ($V_{OC} = 1.04$ V, $J_{SC} = 20.85$ mA/cm², FF = 74.73%) and 17.9% ($V_{OC} = 1.06$ V, $J_{SC} = 21.74$ mA/cm², FF = 77.44 %) for the TTMAI-treated solar cells, respectively.

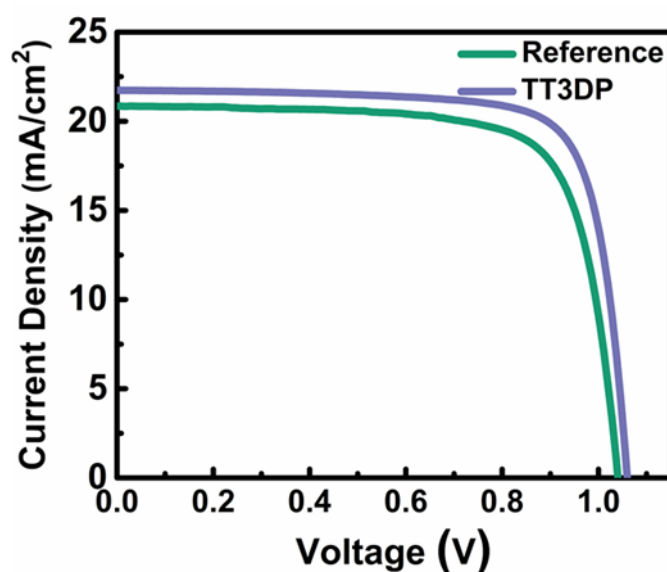


Figure 3.23. J-V curves of the champion reference and TT3DP ST-PSCs.

The integrated J_{sc} results were obtained from EQE measurements and calculated as 20.76 mA/cm² for the reference cell and 21.33 mA/cm² for TT3DP solar cells, respectively (Figure 3.24).

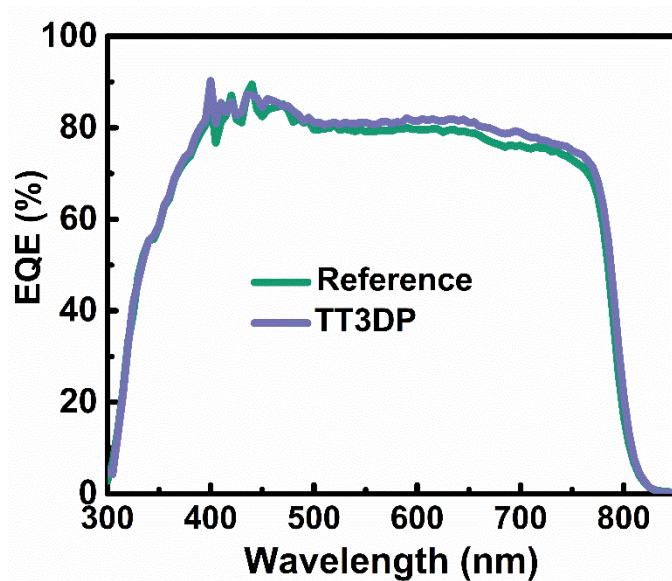


Figure 3.24. EQE spectra of the reference and TT3DP ST-PSCs.

3.4 Stability studies of the opaque and semitransparent solar cells

The stability measurements for both opaque and semitransparent solar cells were performed under the same light intensity (100 mW/s^2) and ambient conditions. The continuous light soaking test and long-term stability measurements were conducted for opaque PSCs, while for semitransparent cells, long-term stability (over 1000 h) measurements were carried out.

3.4.1 Stability Studies of the Opaque PSCs

As mentioned before, high device efficiency and considerable shelf-life are required for the commercialization of solar cells. Perovskite cells suffer from intrinsic and extrinsic instability, even if they outperform their biggest opponents (Si wafer-based solar cells). Intrinsic instability is primarily caused by ionic defects on the perovskite surface, ion deposition at interfaces, and others. On the other hand, UV light, oxygen, and humidity are among the factors that cause the external instability of PSCs. Various studies have been carried out to improve stability. Significant progress has

been made in enhancing the stability of the solar cells by modifying the perovskite/HTL interface by inserting a wide variety of organic ammonium salt layers.

The stability studies were performed to see the effect of the TTMAI layer on stability. First, both reference and TT3DP solar cells were kept under continuous light for 1000 seconds. As seen in Figure 3.25, TT3DP PSCs showed superior stability against light soaking. The drop in efficiency was recorded as 1.5% (17.3% → 15.8%) for reference solar cells and 0.48% (18.5% → 18.02%) for TT3DP solar cell.

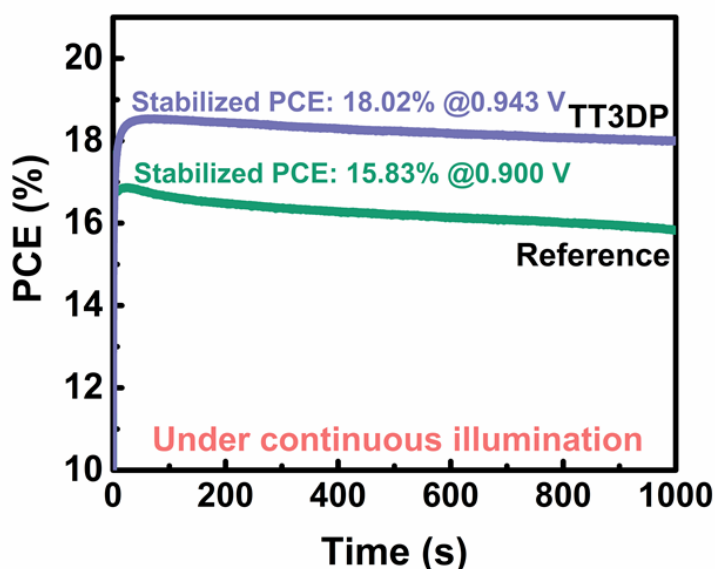


Figure 3.25. Stabilized PCEs of the reference and TT3DP PSCs measured under continuous light at ambient conditions.

The second study was devised to determine the long-term stability of the solar cells. The devices were stored in the desiccator (the relative humidity below 15%) while not measured. It has been observed that the TTMAI-treated solar cell showed superior stability compared to the reference cell. The reference cell maintained only 38% of its initial efficiency, whereas the TT3DP PSC retained 82% of its initial yield after 384 h. It should be noted that devices with the MoO_x layer often suffer from

instability. By the addition of the TTMAI layer, the detrimental effect of the MoO_x layer is greatly reduced.

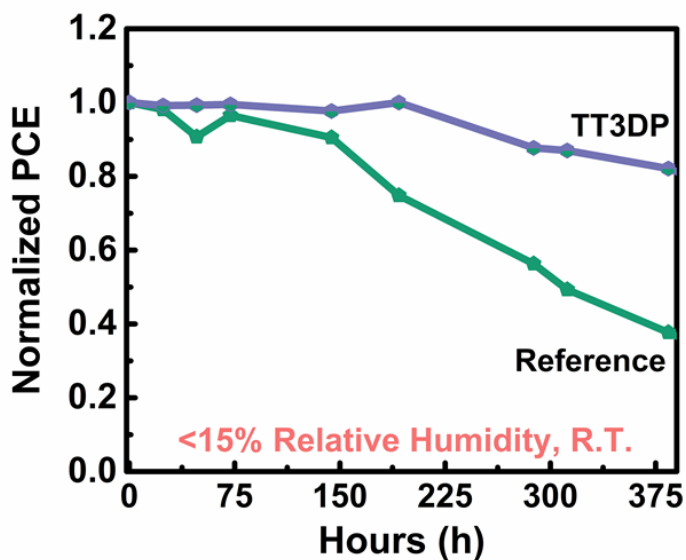


Figure 3.26. Normalized PCEs of the reference and TT3DP PSCs at ambient conditions.

3.4.2 Stability Studies of the ST-PSCs

The long-term stability measurements were conducted for best-performing reference and TT3DP semitransparent solar cells and performed under the same conditions as opaque cell stability measurements. After six weeks from the fabrication, the reference solar cell retained 69% of its initial yield while the TT3DP PSC maintained 87% of the initial PCE (Figure 3.27).

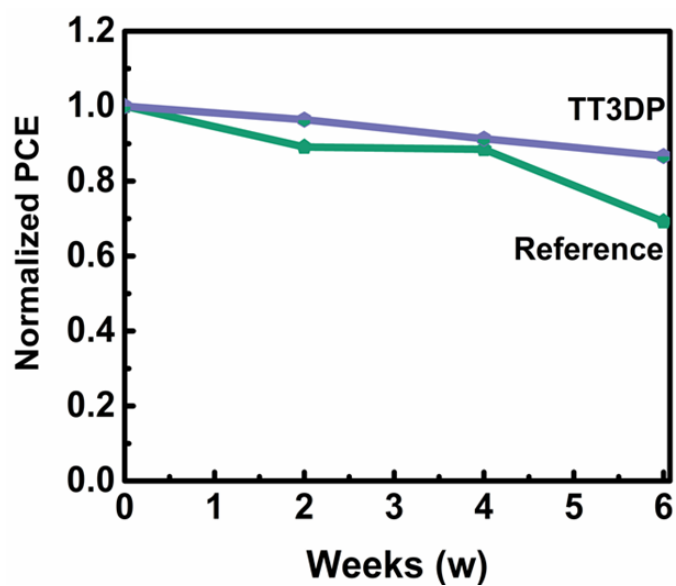


Figure 3.27. Normalized PCE of the reference and TT3DP ST-PSCs kept under the dark at room temperature with <15% relative humidity for six weeks.

CHAPTER 4

CONCLUSION

In the scope of this thesis, novel organic ammonium salt was inserted on a 3D double cationic perovskite aiming to enhance device performance and improve stability. The TT3DP- based solar cells resembled superior device performance to reference perovskite solar cells. Noticeable improvement in FF was obtained with a minor enhancement on J_{sc} and V_{oc} parameters. The PCE of the solar cells increased from 17% to 20%, with a lower hysteresis at different scan rates.

Additionally, the influence of this salt on the perovskite surface was also studied. The GIXRD measurements revealed that although PbI_2 on the surface decreased upon TTMAI insertion, the 2D layer formation was only obtained by 1.5 mg/mL of TTMAI concentration. The other concentrations displayed a formation of an interface layer rather than lowering dimensionality. Additionally, the top-view SEM images showed that the 3D film surface has changed with the salt modification (the layer became smoother), and this change was also supported by the AFM results.

The reason for the significant improvement in FF was explained by both IS and PL measurements indicating that the TTMAI layer provides better charge transport between the 3D perovskite and HTL. Moreover, the valence band of the TTMAI was measured by UPS and showed that the HOMO level of the salt was favorably between the FAMA/HTL interface.

In addition to opaque PSCs, semitransparent solar cells with one of the highest PCEs among FAMA perovskites have been produced. TT3DP ST-PSCs achieved 17.9% of PCE.

Besides efficiency improvement, thanks to the hydrophobic nature of the TTMAI salt, the stability of the PSCs also significantly improved according to contact angle measurements. Based on this observation, stability studies of solar cells were tested. TT3DP solar cell showed remarkable stability under continuous light compared to the reference cell for 1000 s. In addition, their long-term stabilities were also investigated. The TT3DP PSC maintained 82% of the initial PCE, while the reference cell only retained 38% of its initial yield. The stability studies were also conducted for the ST-PSCs as well. The TT3DP ST-PSC retained 87% of the initial PCE, and the reference cell was maintained 69% of its initial efficiency over 1000 h.

REFERENCES

- (1) Roy, P.; Kumar Sinha, N.; Tiwari, S.; Khare, A. A Review on Perovskite Solar Cells: Evolution of Architecture, Fabrication Techniques, Commercialization Issues and Status. *Sol. Energy* **2020**, *198*, 665–688. <https://doi.org/10.1016/J.SOLENER.2020.01.080>.
- (2) Kabir, E.; Kumar, P.; Kumar, S.; Adelodun, A. A.; Kim, K. H. Solar Energy: Potential and Future Prospects. *Renew. Sustain. Energy Rev.* **2018**, *82*, 894–900. <https://doi.org/10.1016/J.RSER.2017.09.094>.
- (3) Sukhatme, S. P.; Nayak, J. K. The Solar Energy Option: An Overview of Thermal Application. *Sol. Energy* **2008**, 37–70.
- (4) Becquerel, A. E.; Memoire Sur Les Effets Electriques Produits Sous l’Influence Des Rayons Solaires. *C. R. Hebd. Seances Acad. Sci.* **1839**, *9*, 561–567.
- (5) Fritts, C.E.; On the Fritts Selenium Cells and Batteries . *Van Nostrands Eng. Mag* **1885**, *32*, 388–395.
- (6) This Month in Physics. *APS NEWS* **2009**, *18* (4), 2.
- (7) Fraunhofer Institute for Solar Energy Systems. Photovoltaics Report. **2021**.
- (8) Zhang, T.; Wang, M.; Yang, H. A Review of the Energy Performance and Life-Cycle Assessment of Building-Integrated Photovoltaic (BIPV) Systems. *Energies* **2018**, *11* (11), 3157. <https://doi.org/10.3390/EN11113157>.
- (9) Polman, A.; Knight, M.; Garnett, E. C.; Ehrler, B.; Sinke, W. C. Photovoltaic Materials: Present Efficiencies and Future Challenges. *Science* (80-.). **2016**, *352* (6283). <https://doi.org/10.1126/SCIENCE.AAD4424>.
- (10) Conibeer, G. Third-Generation Photovoltaics. *Mater. Today* **2007**, *10* (11), 42–50. [https://doi.org/10.1016/S1369-7021\(07\)70278-X](https://doi.org/10.1016/S1369-7021(07)70278-X).

- (11) O'Regan, B.; Grätzel, M. A Low-Cost, High-Efficiency Solar Cell Based on Dye-Sensitized Colloidal TiO₂ Films. *Nat.* 1991 3536346 **1991**, 353 (6346), 737–740. <https://doi.org/10.1038/353737a0>.
- (12) Green, M. A.; Ho-Baillie, A.; Snaith, H. J. The Emergence of Perovskite Solar Cells. *Nat. Photonics* 2014 87 **2014**, 8 (7), 506–514. <https://doi.org/10.1038/nphoton.2014.134>.
- (13) Park, N. G. Perovskite Solar Cells: An Emerging Photovoltaic Technology. *Mater. Today* **2015**, 18 (2), 65–72. <https://doi.org/10.1016/J.MATTOD.2014.07.007>.
- (14) Xing, G.; Mathews, N.; Sun, S.; Lim, S. S.; Lam, Y. M.; Grätzel, M.; Mhaisalkar, S.; Sum, T. C. Long-Range Balanced Electron-and Hole-Transport Lengths in Organic-Inorganic CH₃NH₃PbI₃. *Science* (80-.). **2013**, 342 (6156), 344–347. <https://doi.org/10.1126/science.1243167>.
- (15) Jung, H. S.; Park, N.-G. Perovskite Solar Cells: From Materials to Devices. *Small* **2015**, 11 (1), 10–25. <https://doi.org/10.1002/sml.201402767>.
- (16) Miyata, A.; Mitioglu, A.; Plochocka, P.; Portugall, O.; Wang, J. T. W.; Stranks, S. D.; Snaith, H. J.; Nicholas, R. J. Direct Measurement of the Exciton Binding Energy and Effective Masses for Charge Carriers in Organic-Inorganic Tri-Halide Perovskites. *Nat. Phys.* **2015**, 11 (7), 582–587. <https://doi.org/10.1038/nphys3357>.
- (17) Meng, L.; You, J.; Yang, Y. Addressing the Stability Issue of Perovskite Solar Cells for Commercial Applications. *Nat. Commun.* 2018 91 **2018**, 9 (1), 1–4. <https://doi.org/10.1038/s41467-018-07255-1>.
- (18) Gao, X.; Zhang, X.; Yin, W.; Wang, H.; Hu, Y.; Zhang, Q.; Shi, Z.; Colvin, V. L.; Yu, W. W.; Zhang, Y. Ruddlesden–Popper Perovskites: Synthesis and Optical Properties for Optoelectronic Applications. *Adv. Sci.* **2019**, 6 (22), 1900941. <https://doi.org/10.1002/adv.201900941>.

- (19) Green, M. A.; Ho-Baillie, A.; Snaith, H. J. The Emergence of Perovskite Solar Cells. *Nat. Photonics* **2014**, *8* (7), 506–514.
<https://doi.org/10.1038/nphoton.2014.134>.
- (20) Rajagopal, A.; Yao, K.; Jen, A. K.-Y. Toward Perovskite Solar Cell Commercialization: A Perspective and Research Roadmap Based on Interfacial Engineering. *Adv. Mater.* **2018**, *30* (32), 1800455.
<https://doi.org/10.1002/ADMA.201800455>.
- (21) Kojima, A.; Teshima, K.; Shirai, Y.; Miyasaka, T. Organometal Halide Perovskites as Visible-Light Sensitizers for Photovoltaic Cells. *J. Am. Chem. Soc.* **2009**, *131* (17), 6050–6051. <https://doi.org/10.1021/ja809598r>.
- (22) Im, J.-H.; Lee, C.-R.; Lee, J.-W.; Park, S.-W.; Park, N.-G. 6.5% Efficient Perovskite Quantum-Dot-Sensitized Solar Cell. *Nanoscale* **2011**, *3* (10), 4088–4093. <https://doi.org/10.1039/C1NR10867K>.
- (23) Kim, H.-S.; Lee, C.-R.; Im, J.-H.; Lee, K.-B.; Moehl, T.; Marchioro, A.; Moon, S.-J.; Humphry-Baker, R.; Yum, J.-H.; Moser, J. E.; Grätzel, M.; Park, N.-G. Lead Iodide Perovskite Sensitized All-Solid-State Submicron Thin Film Mesoscopic Solar Cell with Efficiency Exceeding 9%. *Sci. Reports 2012 21* **2012**, *2* (1), 1–7. <https://doi.org/10.1038/srep00591>.
- (24) Lee, M. M.; Teuscher, J.; Miyasaka, T.; Murakami, T. N.; Snaith, H. J. Efficient Hybrid Solar Cells Based on Meso-Superstructured Organometal Halide Perovskites. *Science (80-.)*. **2012**, *338* (6107), 643–647.
<https://doi.org/10.1126/SCIENCE.1228604>.
- (25) Liu, M.; Johnston, M. B.; Snaith, H. J. Efficient Planar Heterojunction Perovskite Solar Cells by Vapour Deposition. *Nat. 2013 5017467* **2013**, *501* (7467), 395–398. <https://doi.org/10.1038/nature12509>.
- (26) Im, J. H.; Jang, I. H.; Pellet, N.; Grätzel, M.; Park, N. G. Growth of CH₃NH₃PbI₃ Cuboids with Controlled Size for High-Efficiency Perovskite Solar Cells. *Nat. Nanotechnol.* **2014**, *9* (11), 927–932.

<https://doi.org/10.1038/nnano.2014.181>.

- (27) Giordano, F.; Abate, A.; Correa Baena, J. P.; Saliba, M.; Matsui, T.; Im, S. H.; Zakeeruddin, S. M.; Nazeeruddin, M. K.; Hagfeldt, A.; Graetzel, M. Enhanced Electronic Properties in Mesoporous TiO₂ via Lithium Doping for High-Efficiency Perovskite Solar Cells. *Nat. Commun.* **2016**, *7*, 1–6. <https://doi.org/10.1038/ncomms10379>.
- (28) Bi, D.; Yi, C.; Luo, J.; Décoppet, J.-D.; Zhang, F.; Zakeeruddin, S. M.; Li, X.; Hagfeldt, A.; Grätzel, M. Polymer-Templated Nucleation and Crystal Growth of Perovskite Films for Solar Cells with Efficiency Greater than 21. **2016**. <https://doi.org/10.1038/NENERGY.2016.142>.
- (29) Jeong, J.; Kim, M.; Seo, J.; Lu, H.; Ahlawat, P.; Mishra, A.; Yang, Y.; Hope, M. A.; Eickemeyer, F. T.; Kim, M.; Yoon, Y. J.; Choi, I. W.; Darwich, B. P.; Choi, S. J.; Jo, Y.; Lee, J. H.; Walker, B.; Zakeeruddin, S. M.; Emsley, L.; Rothlisberger, U.; Hagfeldt, A.; Kim, D. S.; Grätzel, M.; Kim, J. Y. Pseudo-Halide Anion Engineering for α -FAPbI₃ Perovskite Solar Cells. *Nat.* **2021**, *592* (7854), 381–385. <https://doi.org/10.1038/s41586-021-03406-5>.
- (30) Saliba, M.; Correa-Baena, J.-P.; Wolff, C. M.; Stolterfoht, M.; Phung, N.; Albrecht, S.; Neher, D.; Abate, A. How to Make over 20% Efficient Perovskite Solar Cells in Regular (n–i–p) and Inverted (p–i–n) Architectures. *Chem. Mater.* **2018**, *30* (13), 4193–4201. <https://doi.org/10.1021/ACS.CHEMMATER.8B00136>.
- (31) Shi, Z.; Jayatissa, A. H. Perovskites-Based Solar Cells: A Review of Recent Progress, Materials and Processing Methods. *Mater.* **2018**, *11* (5), 729. <https://doi.org/10.3390/MA11050729>.
- (32) Vasiliev, M.; Nur-E-Alam, M.; Alameh, K. Recent Developments in Solar Energy-Harvesting Technologies for Building Integration and Distributed Energy Generation. *Energies* **2019**, *12* (6), 1080.

<https://doi.org/10.3390/en12061080>.

- (33) Shi, B.; Duan, L.; Zhao, Y.; Luo, J.; Zhang, X. Semitransparent Perovskite Solar Cells: From Materials and Devices to Applications. *Adv. Mater.* **2020**, *32* (3), 1806474. <https://doi.org/10.1002/adma.201806474>.
- (34) Rahmany, S.; Etgar, L. Semitransparent Perovskite Solar Cells. *ACS Energy Lett.* **2020**, *5* (5), 1519–1531. <https://doi.org/10.1021/acseenergylett.0c00417>.
- (35) Kranz, L.; Abate, A.; Feurer, T.; Fu, F.; Avancini, E.; Löckinger, J.; Reinhard, P.; Zakeeruddin, S. M.; Grätzel, M.; Buecheler, S.; Tiwari, A. N. High-Efficiency Polycrystalline Thin Film Tandem Solar Cells. *J. Phys. Chem. Lett.* **2015**, *6* (14), 2676–2681. <https://doi.org/10.1021/ACS.JPCLETT.5B01108>.
- (36) Fu, F.; Feurer, T.; Jäger, T.; Avancini, E.; Bissig, B.; Yoon, S.; Buecheler, S.; Tiwari, A. N. Low-Temperature-Processed Efficient Semi-Transparent Planar Perovskite Solar Cells for Bifacial and Tandem Applications. *Nat. Commun.* **2015**, *6* (1), 1–9. <https://doi.org/10.1038/ncomms9932>.
- (37) Tai, Q.; Yan, F. Emerging Semitransparent Solar Cells: Materials and Device Design. *Adv. Mater.* **2017**, *29* (34), 1700192. <https://doi.org/10.1002/ADMA.201700192>.
- (38) Liu, Y.; Hong, Z.; Chen, Q.; Chen, H.; Chang, W.-H.; Yang, Y. M.; Song, T.-B.; Yang, Y. Perovskite Solar Cells Employing Dopant-Free Organic Hole Transport Materials with Tunable Energy Levels. *Adv. Mater.* **2016**, *28* (3), 440–446. <https://doi.org/10.1002/adma.201504293>.
- (39) Yang, D.; Zhang, X.; Hou, Y.; Wang, K.; Ye, T.; Yoon, J.; Wu, C.; Sanghadasa, M.; Liu, S. (Frank); Priya, S. 28.3%-Efficiency Perovskite/Silicon Tandem Solar Cell by Optimal Transparent Electrode for High Efficient Semitransparent Top Cell. *Nano Energy* **2021**, *84*, 105934. <https://doi.org/10.1016/j.nanoen.2021.105934>.

- (40) Chen, B.; Baek, S. W.; Hou, Y.; Aydin, E.; De Bastiani, M.; Scheffel, B.; Proppe, A.; Huang, Z.; Wei, M.; Wang, Y. K.; Jung, E. H.; Allen, T. G.; Van Kerschaver, E.; García de Arquer, F. P.; Saidaminov, M. I.; Hoogland, S.; De Wolf, S.; Sargent, E. H. Enhanced Optical Path and Electron Diffusion Length Enable High-Efficiency Perovskite Tandems. *Nat. Commun.* **2020**, *11* (1), 1–9. <https://doi.org/10.1038/s41467-020-15077-3>.
- (41) Park, H. H.; Kim, J.; Kim, G.; Jung, H.; Kim, S.; Moon, C. S.; Lee, S. J.; Shin, S. S.; Hao, X.; Yun, J. S.; Green, M. A.; Ho-Baillie, A. W. Y.; Jeon, N. J.; Yang, T.; Seo, J. Transparent Electrodes Consisting of a Surface-Treated Buffer Layer Based on Tungsten Oxide for Semitransparent Perovskite Solar Cells and Four-Terminal Tandem Applications. *Small Methods* **2020**, *4* (5), 2000074. <https://doi.org/10.1002/smtd.202000074>.
- (42) Wang, Z.; Zhu, X.; Zuo, S.; Chen, M.; Zhang, C.; Wang, C.; Ren, X.; Yang, Z.; Liu, Z.; Xu, X.; Chang, Q.; Yang, S.; Meng, F.; Liu, Z.; Yuan, N.; Ding, J.; Liu, S. (Frank); Yang, D. 27%-Efficiency Four-Terminal Perovskite/Silicon Tandem Solar Cells by Sandwiched Gold Nanomesh. *Adv. Funct. Mater.* **2020**, *30* (4), 1908298. <https://doi.org/10.1002/adfm.201908298>.
- (43) Yuan, L.; Wang, Z.; Duan, R.; Huang, P.; Zhang, K.; Chen, Q.; Allam, N. K.; Zhou, Y.; Song, B.; Li, Y. Semi-Transparent Perovskite Solar Cells: Unveiling the Trade-off between Transparency and Efficiency. *J. Mater. Chem. A* **2018**, *6* (40), 19696–19702. <https://doi.org/10.1039/c8ta07318j>.
- (44) Duong, T.; Pham, H.; Kho, T. C.; Phang, P.; Fong, K. C.; Yan, D.; Yin, Y.; Peng, J.; Mahmud, M. A.; Gharibzadeh, S.; Nejand, B. A.; Hossain, I. M.; Khan, M. R.; Mozaffari, N.; Wu, Y. L.; Shen, H.; Zheng, J.; Mai, H.; Liang, W.; Samundsett, C.; Stocks, M.; McIntosh, K.; Andersson, G. G.; Lemmer, U.; Richards, B. S.; Paetzold, U. W.; Ho-Baillie, A.; Liu, Y.; Macdonald, D.; Blakers, A.; Wong-Leung, J.; White, T.; Weber, K.; Catchpole, K. High Efficiency Perovskite-Silicon Tandem Solar Cells: Effect of Surface Coating

- versus Bulk Incorporation of 2D Perovskite. *Adv. Energy Mater.* **2020**, *10* (9), 1–15. <https://doi.org/10.1002/aenm.201903553>.
- (45) De Bastiani, M.; Mirabelli, A. J.; Hou, Y.; Gota, F.; Aydin, E.; Allen, T. G.; Troughton, J.; Subbiah, A. S.; Isikgor, F. H.; Liu, J.; Xu, L.; Chen, B.; Van Kerschaver, E.; Baran, D.; Fraboni, B.; Salvador, M. F.; Paetzold, U. W.; Sargent, E. H.; De Wolf, S. Efficient Bifacial Monolithic Perovskite/Silicon Tandem Solar Cells via Bandgap Engineering. *Nat. Energy* **2021**, *6* (2), 167–175. <https://doi.org/10.1038/s41560-020-00756-8>.
- (46) Ramírez Quiroz, C. O.; Shen, Y.; Salvador, M.; Forberich, K.; Schrenker, N.; Spyropoulos, G. D.; Huemueller, T.; Wilkinson, B.; Kirchartz, T.; Spiecker, E.; Verlinden, P. J.; Zhang, X.; Green, M.; Ho-Baillie, A. W. Y.; Brabec, C. J. Balancing Electrical and Optical Losses for Efficient Si-Perovskite 4-Terminal Solar Cells with Solution Processed Percolation Electrodes. *J. Mater. Chem. A* **2018**, *6*, 3583. <https://doi.org/10.1039/C7TA10945H>.
- (47) Boix, P. P.; Raga, S. R.; Mathews, N. Working Principles of Perovskite Solar Cells. In *Halide Perovskites*; Wiley-VCH Verlag GmbH & Co. KGaA, 2018; pp 81–99. https://doi.org/10.1002/9783527800766.ch2_01.
- (48) Yin, W.-J.; Shi, T.; Yan, Y. Unique Properties of Halide Perovskites as Possible Origins of the Superior Solar Cell Performance. *Adv. Mater.* **2014**, *26* (27), 4653–4658. <https://doi.org/10.1002/ADMA.201306281>.
- (49) Pan, H.; Shao, H.; Zhang, X. L.; Shen, Y.; Wang, M. Interface Engineering for High-Efficiency Perovskite Solar Cells. *J. Appl. Phys.* **2021**, *129* (13), 130904. <https://doi.org/10.1063/5.0038073>.
- (50) Zhou, D.; Zhou, T.; Tian, Y.; Zhu, X.; Tu, Y. Perovskite-Based Solar Cells: Materials, Methods, and Future Perspectives. *J. Nanomater.* **2018**, *2018*. <https://doi.org/10.1155/2018/8148072>.
- (51) Solar Cell Parameters and Equivalent Circuit 9.1 External Solar Cell

Parameters.

- (52) PV Education. Series Resistance
<https://www.pveducation.org/pvcdrom/solar-cell-operation/series-resistance>
(accessed Aug 22, 2021).
- (53) You, J.; Meng, L.; Song, T. Bin; Guo, T. F.; Chang, W. H.; Hong, Z.; Chen, H.; Zhou, H.; Chen, Q.; Liu, Y.; De Marco, N.; Yang, Y. Improved Air Stability of Perovskite Solar Cells via Solution-Processed Metal Oxide Transport Layers. *Nat. Nanotechnol.* **2016**, *11* (1), 75–81.
<https://doi.org/10.1038/nnano.2015.230>.
- (54) Asghar, M. I.; Zhang, J.; Wang, H.; Lund, P. D. Device Stability of Perovskite Solar Cells – A Review. *Renew. Sustain. Energy Rev.* **2017**, *77*, 131–146. <https://doi.org/10.1016/J.RSER.2017.04.003>.
- (55) Rong, Y.; Hu, Y.; Mei, A.; Tan, H.; Saidaminov, M. I.; Seok, S. Il; McGehee, M. D.; Sargent, E. H.; Han, H. Challenges for Commercializing Perovskite Solar Cells. *Science (80-.)*. **2018**, *361* (6408).
<https://doi.org/10.1126/SCIENCE.AAT8235>.
- (56) Conings, B.; Drijkoningen, J.; Gauquelin, N.; Babayigit, A.; D’Haen, J.; D’Olieslaeger, L.; Ethirajan, A.; Verbeeck, J.; Manca, J.; Mosconi, E.; Angelis, F. De; Boyen, H.-G. Intrinsic Thermal Instability of Methylammonium Lead Trihalide Perovskite. *Adv. Energy Mater.* **2015**, *5* (15), 1500477. <https://doi.org/10.1002/aenm.201500477>.
- (57) Snaith, H. J.; Abate, A.; Ball, J. M.; Eperon, G. E.; Leijtens, T.; Noel, N. K.; Stranks, S. D.; Tse, J.; Wang, W.; Wojciechowski, K.; Zhang, W. Anomalous Hysteresis in Perovskite Solar Cells. *J. Phys. Chem. Lett* **2014**, *5*, 35. <https://doi.org/10.1021/jz500113x>.
- (58) Wu, F.; Pathak, R.; Qiao, Q. Origin and Alleviation of J-V Hysteresis in Perovskite Solar Cells: A Short Review. *Catal. Today* **2021**, *374*.
<https://doi.org/10.1016/j.cattod.2020.12.025>.

- (59) Chen, B.; Yang, M.; Priya, S.; Zhu, K. Origin of J–V Hysteresis in Perovskite Solar Cells. **2016**. <https://doi.org/10.1021/acs.jpcclett.6b00215>.
- (60) Asghar, M. I.; Zhang, J.; Wang, H.; Lund, P. D. Device Stability of Perovskite Solar Cells – A Review. *Renew. Sustain. Energy Rev.* **2017**, *77*, 131–146. <https://doi.org/10.1016/J.RSER.2017.04.003>.
- (61) Osterwald, C. R.; McMahon, T. J. History of Accelerated and Qualification Testing of Terrestrial Photovoltaic Modules: A Literature Review. *Prog. Photovoltaics Res. Appl.* **2009**, *17* (1), 11–33. <https://doi.org/10.1002/PIP.861>.
- (62) Kim, H.-S.; Seo, J.-Y.; Park, N.-G. Material and Device Stability in Perovskite Solar Cells. *ChemSusChem* **2016**, *9* (18), 2528–2540. <https://doi.org/10.1002/CSSC.201600915>.
- (63) Jeevaraj, M.; Sudhahar, S.; Kumar, M. K. Evolution of Stability Enhancement in Organo-Metallic Halide Perovskite Photovoltaics-A Review. *Mater. Today Commun.* **2021**, 102159. <https://doi.org/10.1016/j.mtcomm.2021.102159>.
- (64) Yan, J.; Qiu, W.; Wu, G.; Heremans, P.; Chen, H. Recent Progress in 2D/Quasi-2D Layered Metal Halide Perovskites for Solar Cells. *J. Mater. Chem. A* **2018**, *6* (24), 11063–11077. <https://doi.org/10.1039/c8ta02288g>.
- (65) Sha, W. E. I.; Ren, X.; Chen, L.; Choy, W. C. H. The Efficiency Limit of CH₃NH₃PbI₃ Perovskite Solar Cells. *Appl. Phys. Lett.* **2015**, *106* (22), 221104. <https://doi.org/10.1063/1.4922150>.
- (66) Ehrler, B.; Alarcón-Lladó, E.; Tabernig, S. W.; Veeken, T.; Garnett, E. C.; Polman, A. Photovoltaics Reaching for the Shockley–Queisser Limit. *ACS Energy Lett.* **2020**, *5* (9), 3029–3033. <https://doi.org/10.1021/ACSENERGYLETT.0C01790>.
- (67) Apurba Mahapatra; Daniel Prochowicz; Mahdi Tavakoli, M.;

- Suvena Trivedi; Pawan Kumar; Pankaj Yadav. A Review of Aspects of Additive Engineering in Perovskite Solar Cells. *J. Mater. Chem. A* **2019**, *8* (1), 27–54. <https://doi.org/10.1039/C9TA07657C>.
- (68) Maria Vasilopoulou; Azhar Fakharuddin; G. Coutsolelos, A.; Polycarpos Falaras; Panagiotis Argitis; Mohd Yusoff, A. R. bin; Khaja Nazeeruddin, M. Molecular Materials as Interfacial Layers and Additives in Perovskite Solar Cells. *Chem. Soc. Rev.* **2020**, *49* (13), 4496–4526. <https://doi.org/10.1039/C9CS00733D>.
- (69) Lu, H.; Krishna, A.; Zakeeruddin, S. M.; Grätzel, M.; Hagfeldt, A. Compositional and Interface Engineering of Organic-Inorganic Lead Halide Perovskite Solar Cells. *iScience* **2020**, *23* (8), 101359. <https://doi.org/10.1016/J.ISCI.2020.101359>.
- (70) Deng, W.; Liang, X.; Kubiak, P. S.; Cameron, P. J. Molecular Interlayers in Hybrid Perovskite Solar Cells. *Adv. Energy Mater.* **2018**, *8* (1), 1701544. <https://doi.org/10.1002/AENM.201701544>.
- (71) Liang, L.; Luo, H.; Hu, J.; Li, H.; Gao, P. Efficient Perovskite Solar Cells by Reducing Interface-Mediated Recombination: A Bulky Amine Approach. *Adv. Energy Mater.* **2020**, *10* (14), 2000197. <https://doi.org/10.1002/AENM.202000197>.
- (72) Zhang, J.; Yu, H. Reduced Energy Loss Enabled by Thiophene-Based Interlayers for High Performance and Stable Perovskite Solar Cells. *J. Mater. Chem. A* **2021**, *9* (7), 4138–4149. <https://doi.org/10.1039/D0TA10270A>.
- (73) Noel, N. K.; Abate, A.; Stranks, S. D.; Parrott, E. S.; Burlakov, V. M.; Goriely, A.; Snaith, H. J. Enhanced Photoluminescence and Solar Cell Performance via Lewis Base Passivation of Organic–Inorganic Lead Halide Perovskites. *ACS Nano* **2014**, *8* (10), 9815–9821. <https://doi.org/10.1021/NN5036476>.

- (74) Wen, T. Y.; Yang, S.; Liu, P. F.; Tang, L. J.; Qiao, H. W.; Chen, X.; Yang, X. H.; Hou, Y.; Yang, H. G. Surface Electronic Modification of Perovskite Thin Film with Water-Resistant Electron Delocalized Molecules for Stable and Efficient Photovoltaics. *Adv. Energy Mater.* **2018**, *8* (13).
<https://doi.org/10.1002/aenm.201703143>.
- (75) Lin, Y.; Shen, L.; Dai, J.; Deng, Y.; Wu, Y.; Bai, Y.; Zheng, X.; Wang, J.; Fang, Y.; Wei, H.; Ma, W.; Zeng, X. C.; Zhan, X.; Huang, J. π -Conjugated Lewis Base: Efficient Trap-Passivation and Charge-Extraction for Hybrid Perovskite Solar Cells. *Adv. Mater.* **2017**, *29* (7), 1604545.
<https://doi.org/10.1002/ADMA.201604545>.
- (76) Kim, S.-G.; Le, T. H.; Monfreid, T. de; Goubard, F.; Bui, T.-T.; Park, N.-G. Capturing Mobile Lithium Ions in a Molecular Hole Transporter Enhances the Thermal Stability of Perovskite Solar Cells. *Adv. Mater.* **2021**, *33* (12), 2007431. <https://doi.org/10.1002/ADMA.202007431>.
- (77) Zhao, B.; Yan, X.; Zhang, T.; Ma, X.; Liu, C.; Liu, H.; Yan, K.; Chen, Y.; Li, X. Introduction of Multifunctional Triphenylamino Derivatives at the Perovskite/HTL Interface to Promote Efficiency and Stability of Perovskite Solar Cells. *ACS Appl. Mater. Interfaces* **2020**, *12* (8), 9300–9306.
<https://doi.org/10.1021/acsami.9b21112>.
- (78) I., D.; InabeTamotsu; MaruyamaYusei. In Situ X-Ray Observation on the Intercalation of Weak Interaction Molecules into Perovskite-Type Layered Crystals (C₉H₁₉NH₃)₂PbI₄ and (C₁₀H₂₁NH₃)₂CdCl₄.
<http://dx.doi.org/10.1246/bcsj.59.563> **2006**, *59* (2), 563–567.
<https://doi.org/10.1246/BCSJ.59.563>.
- (79) Smith, I. C.; Hoke, E. T.; Solis-Ibarra, D.; McGehee, M. D.; Karunadasa, H. I. A Layered Hybrid Perovskite Solar-Cell Absorber with Enhanced Moisture Stability. *Angew. Chemie Int. Ed.* **2014**, *53* (42), 11232–11235.
<https://doi.org/10.1002/ANIE.201406466>.

- (80) Lai, X.; Li, W.; Gu, X.; Chen, H.; Zhang, Y.; Li, G.; Zhang, R.; Fan, D.; He, F.; Zheng, N.; Yu, J.; Chen, R.; Kyaw, A. K. K.; Sun, X. W. High-Performance Quasi-2D Perovskite Solar Cells with Power Conversion Efficiency over 20% Fabricated in Humidity-Controlled Ambient Air. *Chem. Eng. J.* **2022**, *427*, 130949. <https://doi.org/10.1016/J.CEJ.2021.130949>.
- (81) Cheng, Z.; Lin, J. Layered Organic-Inorganic Hybrid Perovskites: Structure, Optical Properties, Film Preparation, Patterning and Templating Engineering. *CrystEngComm* **2010**, *12* (10), 2646–2662. <https://doi.org/10.1039/c001929a>.
- (82) Xu, Y.; Wang, M.; Lei, Y.; Ci, Z.; Jin, Z. Crystallization Kinetics in 2D Perovskite Solar Cells. *Adv. Energy Mater.* **2020**, *10* (43), 1–18. <https://doi.org/10.1002/aenm.202002558>.
- (83) Thrithamarassery Gangadharan, D.; Ma, D. Searching for Stability at Lower Dimensions: Current Trends and Future Prospects of Layered Perovskite Solar Cells. *Energy Environ. Sci.* **2019**, *12* (10), 2860–2889. <https://doi.org/10.1039/c9ee01591d>.
- (84) Grancini, G.; Nazeeruddin, M. K. Dimensional Tailoring of Hybrid Perovskites for Photovoltaics. *Nat. Rev. Mater.* **2018**, *4* (1), 4–22. <https://doi.org/10.1038/s41578-018-0065-0>.
- (85) Mao, L.; Stoumpos, C. C.; Kanatzidis, M. G. Two-Dimensional Hybrid Halide Perovskites: Principles and Promises. *J. Am. Chem. Soc.* **2019**, *141* (3), 1171–1190. <https://doi.org/10.1021/jacs.8b10851>.
- (86) Ortiz-Cervantes, C.; Carmona-Monroy, P.; Solis-Ibarra, D. Two-Dimensional Halide Perovskites in Solar Cells: 2D or Not 2D? *ChemSusChem* **2019**, *12* (8), 1560–1575. <https://doi.org/10.1002/cssc.201802992>.
- (87) Cheng, Z.; Lin, J. Layered Organic–Inorganic Hybrid Perovskites: Structure,

Optical Properties, Film Preparation, Patterning and Templating Engineering. *CrystEngComm* **2010**, *12* (10), 2646–2662.
<https://doi.org/10.1039/C001929A>.

- (88) Ishihara, T.; Takahashi, J.; Goto, T. Exciton State in Two-Dimensional Perovskite Semiconductor (C₁₀H₂₁NH₃)₂PbI₄. *Solid State Commun.* **1989**, *69* (9), 933–936. [https://doi.org/10.1016/0038-1098\(89\)90935-6](https://doi.org/10.1016/0038-1098(89)90935-6).
- (89) Tanaka, K.; Kondo, T. Bandgap and Exciton Binding Energies in Lead-Iodide-Based Natural Quantum-Well Crystals. *Sci. Technol. Adv. Mater.* **2003**, *4* (6), 599–604. <https://doi.org/10.1016/j.stam.2003.09.019>.
- (90) Shao, S.; Loi, M. A. Advances and Prospective in Metal Halide Ruddlesden–Popper Perovskite Solar Cells. *Adv. Energy Mater.* **2021**, 2003907. <https://doi.org/10.1002/aenm.202003907>.
- (91) Ma, C.; Leng, C.; Ji, Y.; Wei, X.; Sun, K.; Tang, L.; Yang, J.; Luo, W.; Li, C.; Deng, Y.; Feng, S.; Shen, J.; Lu, S.; Du, C.; Shi, H. 2D/3D Perovskite Hybrids as Moisture-Tolerant and Efficient Light Absorbers for Solar Cells. *Nanoscale* **2016**, *8* (43), 18309–18314. <https://doi.org/10.1039/c6nr04741f>.
- (92) Grancini, G.; Roldán-Carmona, C.; Zimmermann, I.; Mosconi, E.; Lee, X.; Martineau, D.; Narbey, S.; Oswald, F.; De Angelis, F.; Graetzel, M.; Nazeeruddin, M. K. One-Year Stable Perovskite Solar Cells by 2D/3D Interface Engineering. *Nat. Commun.* **2017**, *8*. <https://doi.org/10.1038/ncomms15684>.
- (93) Liu, Y.; Akin, S.; Pan, L.; Uchida, R.; Arora, N.; Milić, J. V.; Hinderhofer, A.; Schreiber, F.; Uhl, A. R.; Zakeeruddin, S. M.; Hagfeldt, A.; Ibrahim Dar, M.; Grätzel, M. Ultrahydrophobic 3D/2D Fluoroarene Bilayer-Based Water-Resistant Perovskite Solar Cells with Efficiencies Exceeding 22%. *Sci. Adv.* **2019**, *5* (6), 1–9. <https://doi.org/10.1126/sciadv.aaw2543>.
- (94) Wei, M.; Xiao, K.; Walters, G.; Lin, R.; Zhao, Y.; Saidaminov, M. I.; Todorović, P.; Johnston, A.; Huang, Z.; Chen, H.; Li, A.; Zhu, J.; Yang, Z.;

- Wang, Y.; Proppe, A. H.; Kelley, S. O.; Hou, Y.; Voznyy, O.; Tan, H.; Sargent, E. H. Combining Efficiency and Stability in Mixed Tin–Lead Perovskite Solar Cells by Capping Grains with an Ultrathin 2D Layer. *Adv. Mater.* **2020**, *32* (12), 1907058. <https://doi.org/10.1002/adma.201907058>.
- (95) Liu, C.; Sun, J.; Tan, W. L.; Lu, J.; Gengenbach, T. R.; McNeill, C. R.; Ge, Z.; Cheng, Y. B.; Bach, U. Alkali Cation Doping for Improving the Structural Stability of 2D Perovskite in 3D/2D PSCs. *Nano Lett.* **2020**, *20* (2), 1240–1251. <https://doi.org/10.1021/acs.nanolett.9b04661>.
- (96) Lv, Y.; Song, X.; Yin, Y.; Feng, Y.; Ma, H.; Hao, C.; Jin, S.; Shi, Y. Hexylammonium Iodide Derived Two-Dimensional Perovskite as Interfacial Passivation Layer in Efficient Two-Dimensional/Three-Dimensional Perovskite Solar Cells. *ACS Appl. Mater. Interfaces* **2020**, *12* (1), 698–705. <https://doi.org/10.1021/acsami.9b17930>.
- (97) Yao, Q.; Xue, Q.; Li, Z.; Zhang, K.; Zhang, T.; Li, N.; Yang, S.; Brabec, C. J.; Yip, H.; Cao, Y. Graded 2D/3D Perovskite Heterostructure for Efficient and Operationally Stable MA-Free Perovskite Solar Cells. *Adv. Mater.* **2020**, *32* (26), 2000571. <https://doi.org/10.1002/adma.202000571>.
- (98) Jin, S.; Wei, Y.; Rong, B.; Fang, Y.; Zhao, Y.; Guo, Q.; Huang, Y.; Fan, L.; Wu, J. Improving Perovskite Solar Cells Photovoltaic Performance Using Tetrabutylammonium Salt as Additive. *J. Power Sources* **2020**, *450* (December 2019), 227623. <https://doi.org/10.1016/j.jpowsour.2019.227623>.
- (99) Youn, J.; Huang, P.-Y.; Huang, Y.-W.; Chen, M.-C.; Lin, Y.-J.; Huang, H.; Ortiz, R. P.; Stern, C.; Chung, M.-C.; Feng, C.-Y.; Chen, L.-H.; Facchetti, A.; Marks, T. J. Versatile α,ω -Disubstituted Tetrathienoacene Semiconductors for High Performance Organic Thin-Film Transistors. *Adv. Funct. Mater.* **2012**, *22* (1), 48–60. <https://doi.org/10.1002/adfm.201101053>.
- (100) Zhou, T.; Lai, H.; Liu, T.; Lu, D.; Wan, X.; Zhang, X.; Liu, Y.; Chen, Y. Highly Efficient and Stable Solar Cells Based on Crystalline Oriented

- 2D/3D Hybrid Perovskite. *Adv. Mater.* **2019**, *31* (32), 1901242.
<https://doi.org/10.1002/adma.201901242>.
- (101) Sutanto, A. A.; Drigo, N.; Queloz, V. I. E.; Garcia-Benito, I.; Kirmani, A. R.; Richter, L. J.; Schouwink, P. A.; Cho, K. T.; Paek, S.; Nazeeruddin, M. K.; Grancini, G. Dynamical Evolution of the 2D/3D Interface: A Hidden Driver behind Perovskite Solar Cell Instability. *J. Mater. Chem. A* **2020**, *8* (5), 2343–2348. <https://doi.org/10.1039/c9ta12489f>.
- (102) Sutanto, A. A.; Caprioglio, P.; Drigo, N.; Hofstetter, Y. J.; Garcia-Benito, I.; Queloz, V. I. E.; Neher, D.; Nazeeruddin, M. K.; Stolterfoht, M.; Vaynzof, Y.; Grancini, G. 2D/3D Perovskite Engineering Eliminates Interfacial Recombination Losses in Hybrid Perovskite Solar Cells. *Chem* **2021**.
<https://doi.org/10.1016/j.chempr.2021.04.002>.
- (103) Ananda, W. External Quantum Efficiency Measurement of Solar Cell. *QiR 2017 - 2017 15th Int. Conf. Qual. Res. Int. Symp. Electr. Comput. Eng.* **2017**, *2017-December*, 450–456. <https://doi.org/10.1109/QIR.2017.8168528>.
- (104) Holzwarth, U.; Gibson, N. The Scherrer Equation versus the “Debye-Scherrer Equation.” *Nat. Nanotechnol.* *2011 69* **2011**, *6* (9), 534–534.
<https://doi.org/10.1038/nnano.2011.145>.
- (105) Petrus, M. L.; Schlipf, J.; Li, C.; Gujar, T. P.; Giesbrecht, N.; Müller-Buschbaum, P.; Thelakkat, M.; Bein, T.; Hüttner, S.; Docampo, P. Capturing the Sun: A Review of the Challenges and Perspectives of Perovskite Solar Cells. *Adv. Energy Mater.* **2017**, *7* (16), 1700264.
<https://doi.org/10.1002/AENM.201700264>.
- (106) Wang, M.; Lei, Y.; Xu, Y.; Han, L.; Ci, Z.; Jin, Z. The J–V Hysteresis Behavior and Solutions in Perovskite Solar Cells. *Sol. RRL* **2020**, *4* (12), 2000586. <https://doi.org/10.1002/SOLR.202000586>.
- (107) Bou, A.; Pockett, A.; Raptis, D.; Watson, T.; Carnie, M. J.; Bisquert, J. Beyond Impedance Spectroscopy of Perovskite Solar Cells: Insights from

- the Spectral Correlation of the Electrooptical Frequency Techniques. *J. Phys. Chem. Lett.* **2020**, *11* (20), 8654–8659.
<https://doi.org/10.1021/ACS.JPCLETT.0C02459>.
- (108) Kagan, C. R.; Mitzi, D. B.; Dimitrakopoulos, C. D. Organic-Inorganic Hybrid Materials as Semiconducting Channels in Thin-Film Field-Effect Transistors. *Science* (80-.). **1999**, *286* (5441), 945–947.
<https://doi.org/10.1126/science.286.5441.945>.
- (109) Quan, L. N.; Yuan, M.; Comin, R.; Voznyy, O.; Beauregard, E. M.; Hoogland, S.; Buin, A.; Kirmani, A. R.; Zhao, K.; Amassian, A.; Kim, D. H.; Sargent, E. H. Ligand-Stabilized Reduced-Dimensionality Perovskites. *J. Am. Chem. Soc.* **2016**, *138* (8), 2649–2655.
<https://doi.org/10.1021/jacs.5b11740>.
- (110) Proppe, A. H.; Wei, M.; Chen, B.; Quintero-Bermudez, R.; Kelley, S. O.; Sargent, E. H. Photochemically Cross-Linked Quantum Well Ligands for 2D/3D Perovskite Photovoltaics with Improved Photovoltage and Stability. *J. Am. Chem. Soc.* **2019**, *141* (36), 14180–14189.
<https://doi.org/10.1021/jacs.9b05083>.
- (111) Zhou, J.; Ye, Z.; Hou, J.; Wu, J.; Zheng, Y. Z.; Tao, X. Efficient Ambient-Air-Stable HTM-Free Carbon-Based Perovskite Solar Cells with Hybrid 2D-3D Lead Halide Photoabsorbers. *J. Mater. Chem. A* **2018**, *6* (45), 22626–22635. <https://doi.org/10.1039/c8ta07836j>.

